Published in final edited form as:

Inorg Chem. 2018 February 19; 57(4): 1988–2001. doi:10.1021/acs.inorgchem.7b02903.

Sterically Stabilized Terminal Hydride of a Diiron Dithiolate

Michaela R. Carlson,
School of Chemical Sciences, University of Illinois, Urbana, Illinois 61801, United States

Danielle L. Gray,
School of Chemical Sciences, University of Illinois, Urbana, Illinois 61801, United States

Casseday P. Richers,
School of Chemical Sciences, University of Illinois, Urbana, Illinois 61801, United States

Wenguang Wang[†],
School of Chemical Sciences, University of Illinois, Urbana, Illinois 61801, United States

Pei-Hua Zhao[‡],
School of Chemical Sciences, University of Illinois, Urbana, Illinois 61801, United States

Thomas B. Rauchfuss[*],
School of Chemical Sciences, University of Illinois, Urbana, Illinois 61801, United States

Vladimir Pelmenschikov[*],
Institut für Chemie, Technische Universität Berlin, 10623 Berlin, Germany

Cindy C. Pham,
Department of Chemistry, University of California, Davis, California 95616, United States

[*]**Corresponding Authors:** T.B.R.: rauchfuz@illinois.edu.; V.P.: pelmentschikov@tu-berlin.de.; S.P.C.: spjcramer@ucdavis.edu.
[†]**Present Address:** W.W.: School of Chemistry and Chemical Engineering, Shandong University, Jinan 2500100, People's Republic of China.
[‡]**Present Address:** P.-H.Z.: School of Materials and Science Engineering, North University of China, Taiyuan 030051, People's Republic of China

Supporting Information

The Supporting Information is available free of charge on the ACS Publications website at DOI: 10.1021/acs.inorgchem.7b02903.
ESI-MS, FT-IR, NMR, CV, NRVS, and DFT figures and tables; supplementary discussions on the NRVS and DFT results (PDF)
Animated vibrational normal modes (ZIP)
Coordinates of the DFT models (ZIP)

Accession Codes

CCDC 1583878–1583879 contain the supplementary crystallographic data for this paper. These data can be obtained free of charge via www.ccdc.cam.ac.uk/data_request/cif, or by emailing data_request@ccdc.cam.ac.uk, or by contacting The Cambridge Crystallographic Data Centre, 12 Union Road, Cambridge CB2 1EZ, UK; fax: +44 1223 336033.

ORCID

Danielle L. Gray: 0000-0003-0059-2096
Wenguang Wang: 0000-0002-4108-7865
Pei-Hua Zhao: 0000-0002-5480-6128
Thomas B. Rauchfuss: 0000-0003-2547-5128
Vladimir Pelmenschikov: 0000-0002-0523-4418

Author Contributions

T.B.R. and S.P.C. planned the research and designed experiments. M.R.C., C.P.R., W.W., and P.-H.Z. carried out synthetic operations and preliminary characterizations. D.L.G. conducted the X-ray crystallography. C.C.P., L.B.G., and H.W. collected the NRVS data. V.P. carried out the DFT calculations and interpreted their results. T.B.R., V.P., M.R.C., and C.C.P. wrote the manuscript.

Notes

The authors declare no competing financial interest.

Leland B. Gee,
Department of Chemistry, University of California, Davis, California 95616, United States

Hongxin Wang, and
Department of Chemistry, University of California, Davis, California 95616, United States

Stephen P. Cramer*
Department of Chemistry, University of California, Davis, California 95616, United States

Abstract

The kinetically robust hydride [*t*-HFe$_2$(Me$_2$pdt)(CO)$_2$(dppv)$_2$]$^+$ ([*t*-H**1**]$^+$) (Me$_2$pdt^{2-} = Me$_2$C-(CH$_2$S$^-$)$_2$; dppv = *cis*-1,2-C$_2$H$_2$(PPh$_2$)$_2$) and related derivatives were prepared with ^{57}Fe enrichment for characterization by NMR, FT-IR, and NRVS. The experimental results were rationalized using DFT molecular modeling and spectral simulations. The spectroscopic analysis was aimed at supporting assignments of Fe–H vibrational spectra as they relate to recent measurements on [FeFe]-hydrogenase enzymes. The combination of bulky Me$_2$pdt^{2-} and dppv ligands stabilizes the terminal hydride with respect to its isomerization to the 5–16 kcal/mol more stable bridging hydride ([μ-H**1**]$^+$) with $t_{1/2}$(313.3 K) = 19.3 min. In agreement with the nOe experiments, the calculations predict that one methyl group in [*t*-H**1**]$^+$ interacts with the hydride with a computed CH···HFe distance of 1.7 Å. Although [*t*-H^{57}**1**]$^+$ exhibits multiple NRVS features in the 720–800 cm^{-1} region containing the bending Fe–H modes, the deuterated [*t*-D^{57}**1**]$^+$ sample exhibits a unique Fe-D/CO band at ~600 cm^{-1}. In contrast, the NRVS spectra for [μ-H^{57}**1**]$^+$ exhibit weaker bands near 670–700 cm^{-1} produced by the Fe–H–Fe wagging modes coupled to Me$_2$pdt^{2-} and dppv motions.

Graphical abstract

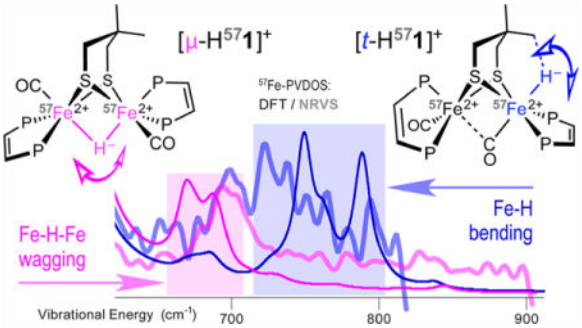

INTRODUCTION

Currently the hydrogenases (H$_2$ases) are receiving much interest because these enzymes exhibit unusual and highly efficient pathways for activating and producing H$_2$.[1–3] It has been long assumed that all hydrogenases operate via the intermediacy of metal hydrides,[4] which are otherwise elusive in nature.[5–8] Such intermediates have long been directly detected for the [NiFe]-H$_2$ases.[9] For the [FeFe]-H$_2$ases, hydrides were initially spectroscopically implicated by the effect of H/D exchange on ν_{CO} bands in the FT-IR spectra.[10,11] The

terminal hydrides have only recently been detected directly, first in mutant proteins[12–14] and more recently in two native proteins (Scheme 1).[15]

For the investigation of iron hydrides, nuclear resonance vibrational spectroscopy (NRVS) is the premier technique[14,17] and, in combination with density functional theory (DFT), was central in our recent direct detection of Fe–H-containing intermediates in the [FeFe]-H_2ases.[14,15]

Biomimetic terminal hydrides participate in two reactions that complicate their analysis. When the dithiolate is the azadithiolate (adt) cofactor (or its N-substituted derivatives), the hydride can be reversibly deprotonated by amine. This effect is illustrated by the case of [*term*-HFe_2(adt)-$(CO)_2(dppv)_2]^+$ (adt = azadithiolate), where the tautomerization is affected by the nature and concentration of the counteranion.[18] Regardless of the nature of the dithiolate bridge, terminal Fe–H hydrides tend to isomerize irreversibly to bridging Fe–H–Fe hydrides.[1] We sought to suppress this reaction, since these bridging hydrides are not relevant to the biological function of [FeFe]-H_2ases.[19]

Many studies have been reported on diiron dithiolates with “rotated structures”. The rotated motif is readily achieved with mixed-valence Fe(II)Fe(I) complexes, but Fe(I)Fe(I) compounds almost invariably adopt the C_{2v} (idealized) structure (Scheme 2). Fe(I)Fe(I) derivatives can also be stabilized in a rotated geometry using bulky dithiolates such as $R_2C(CH_2S^-)_2$ ($R \neq H$).[20–23] In this work, we extend that concept, showing that $Me_2C(CH_2S^-)_2$ also stabilizes terminal hydride species, greatly slowing their isomerization to bridging hydrides. This approach worked so well that we proceeded to collect NRVS data on both the terminal and bridging hydrides. These results are relevant to benchmarking recent NRVS results on the enzyme.[15]

A few comments on “flippamers” are required, since this kind of isomerism occurs in compounds discussed in this paper. Flippamers are conformers of the triatomic backbone of 1,3-propanedithiolate and related $X(CH_2S^-)_2$ bridging ligands in complexes of the type μ-(μ-$X(CH_2S)_2$)[FeL_3]$_2$. The population of the two flippamers depends on the steric similarity of two FeL_3 modules. The flipping rate is fast on the NMR time scale but slow on the EPR and IR time scales.[24]

RESULTS AND DISCUSSION

Characterization of $Fe_2(Me_2pdt)(CO)_2(dppv)_2$ Using FT-IR and NMR Spectroscopy

UV irradiation of a solution of $Fe_2(Me_2pdt)(CO)_4$(dppv)[20] and dppv efficiently gave $Fe_2(Me_2pdt)(CO)_2(dppv)_2$ ([**1**]^0). This compound was obtained as a dark green solid that is mildly sensitive to air and exhibits good solubility in several organic solvents. The FT-IR spectrum revealed intense ν_{CO} bands at 1898 and 1865 cm^{-1} that match well with those (1888, 1868 cm^{-1}) for Fe_2(pdt)-$(CO)_2(dppv)_2$ (Figure S2).[25]

The ^{1}H NMR spectrum of [**1**]^0 shows a methylene signal at δ 1.23, which also matches that for $Fe_2(pdt)(CO)_2(dppv)_2$. The methyl resonance, a broad singlet, is found at δ −0.15 (Figure S3). In contrast, the two Me resonances from the apical/basal and basal/basal

isomers of $Fe_2(Me_2pdt)(CO)_4(dppv)$ absorb at δ 0.98 and 1.08, and the Me resonances of $Fe_2(Me_2pdt)(CO)_6$ absorb at δ 0.98.[20] The upfield shift for the methyl ^{1}H NMR signal $[\mathbf{1}]^0$ is attributed to ring current effects resulting from interactions between the methyl groups and the phenyl groups of the ligand.

The room-temperature ^{31}P NMR spectrum of $[\mathbf{1}]^0$ consists of a singlet at δ 87.0 (Figure S4). At lower temperatures, this signal splits into two singlets, and below −90 °C these singlets broaden further (Figure S6). However, the signal for the methyl groups remains coalesced even at −90 °C (Figure S5). The chemical shift difference for the ^{31}P NMR signals in the slow exchange limit is δ 13.4, corresponding to 2707 Hz (202 MHz observing frequency). The estimated ^{1}H chemical shift difference between unique methyl signals is 2 ppm, corresponding to 1000 Hz (500 MHz). Therefore, the turnstile rotation of the two Fe(CO)(dppv) centers is slower than the flipping of the $[Me_2pdt]^{2-}$ ligand.

Structure of $Fe_2(Me_2pdt)(CO)_2(dppv)_2$

The structure of $[\mathbf{1}]^0$, which crystallizes with a disordered molecule of CH_2Cl_2, was confirmed by X-ray crystallography. The overall structure was similar to that of many $Fe_2(SR)_2L_6$ compounds with an Fe–Fe bond distance of 2.594(1) Å (Figure 1).[1] The crystallographic analysis reveals that the coordination sphere of one Fe is highly distorted. In most compounds of the type $Fe_2(SR)_2L_6$, terminal ligands on the two Fe centers are eclipsed (i.e., torsion angle of 0°), whereas in $[\mathbf{1}]^0$ the P_{apical}–Fe–Fe–P_{apical} torsion angle is 66.43°.[26] In the related diiron complex $Fe_2(Me_2pdt)(CO)_4(PMe_3)_2$, the P_{apical}–Fe–Fe–P_{apical} torsion angle is 28.9°,[21] the smaller angle reflecting the diminished bulk of PMe_3. Since the ν_{CO} values for $[\mathbf{1}]^0$ and $Fe_2(pdt)$-$(CO)_2(dppv)_2$ match well,[25] the distortion observed in the solid state appears not to predominate in solution.

Synthesis of Labeled $^{57}FeFe(Me_2pdt)(CO)_2(dppv)_2$

Also prepared in this work were ^{57}Fe-labeled complexes, which are suitable for characterization by ^{57}Fe-NRVS (see below). To conserve on ^{57}Fe, we targeted derivatives of the $[H\mathbf{1}]^+$ hydride species where half of the iron was ^{57}Fe (Scheme 3). To prepare such "half-labeled" complexes, a ^{57}Fe(II) dithiolate precursor was condensed with an unlabeled Fe(0) reagent. The ferrous building block $^{57}Fe(Me_2pdt)(CO)_2(dppv)$ was prepared in good yield by the reaction of $^{57}FeCl_2$, dppv, and Li_2Me_2pdt under an atmosphere of CO. Although $Fe(Me_2pdt)(CO)_2(dppv)$ has not been reported, the closely related $Ph_2PC_2H_4PPh_2$-containing analogue is known.[27] The ^{31}P NMR spectrum indicates a pair of isomers in a ratio of 17:1. The most abundant isomer has trans carbonyls, while the other isomer carbonyls are cis and the diphosphine exhibits two ^{31}P NMR signals (Figure S33). The trans:cis ratio for the related but less bulky species $Fe(pdt)(CO)_2(dppv)$ is 4:1.[27] The trans isomer is apparently favored by the bulkiness of the Me_2pdt^{2-} ligand. IR spectra for $^{57}Fe(Me_2pdt)(CO)_2(dppv)$ and $Fe(pdt)$-$(CO)_2(dppv)$ are indistinguishable (Table S1).

Treatment of $^{57}Fe(Me_2pdt)(CO)_2(dppv)$ with $Fe(bda)$-$(CO)_3$[28] gave $(CO)_3Fe(Me_2pdt)^{57}Fe(CO)(dppv)$ (bda = benzylideneacetone). In this diiron compound, dppv remains exclusively coordinated to ^{57}Fe, as revealed by the observation of the doublet $J(^{31}P,^{57}Fe)$ = 50.9 Hz in the ^{31}P NMR spectrum (Figure S36). This result indicates the

absence of scrambling of the diphosphine. UV irradiation of a solution of this tetracarbonyl with dppv gave ^{57}FeFe(Me_2pdt)$(CO)_2$(dppv)$_2$ ([^{57}**1**]^0). The ^{31}P NMR spectrum of [^{57}**1**]^0 is characterized by a broad singlet at δ 87.2, which is similar in line shape to that of unlabeled [**1**]^0 (Figure S38).

Electrochemistry of [1]^0

Cyclic voltammetry studies on CH_2Cl_2 solutions of [**1**]^0 show a reversible oxidation at −1.04 V (all potentials are referenced vs $Fc^{+/0}$, Figure S8). With a redox couple at −0.83 V, Fe_2(pdt)$(CO)_2$(dppv)$_2$ is a poorer reductant than [**1**]^0 by ~210 mV. This trend is consistent with steric stabilization of the oxidized product (see below), whose rotated geometry accommodates one of the methyl groups of the Me_2pdt^{2-} ligand. In the case of [Fe_2(R_2pdt)-$(CO)_4(PMe_3)_2$]$^{0/+}$, the effect of pdt^{2-} vs Me_2pdt^{2-} is very similar: 240 mV.[29]

Characterization of [Fe_2(Me_2pdt)$(CO)_2$(dppv)$_2$]$^+$

Oxidation of [**1**]^0 with $FcBF_4$ (Fc = [Fe$(C_5H_5)_2$]$^+$) gave the mixed-valence salt [**1**]BF_4 (Figure 2). As for previously reported Fe(II)Fe(I) species, [**1**]$^+$ is structurally related to the H_{ox} state of [FeFe]-H_2ase.[12,30–36] [**1**]BF_4 is analogous to [Fe_2(pdt)-$(CO)_2$(dppv)$_2$]$^+$.[37]. Crystallographic characterization of [**1**]BF_4 confirmed that [**1**]$^+$ adopts the rotated structure characteristic of these mixed-valence species. One CO ligand is semi-bridging, with Fe_p–C and Fe_d–C distances of 2.461(2) and 1.790(6) Å, respectively. The dppv bound to the rotated iron occupies dibasal positions, whereas the dppv ligand on the second iron (Fe_p) occupies an apical-basal configuration, reminiscent of the location of the two donor ligands on the proximal Fe (Fe_p) in the enzyme. The Fe–P bonds are similar for Fe_p vs Fe_d (2.213(2)/ 2.243(2) Å vs 2.236(2)/2.254(1) Å, respectfully). The crystal structure also reveals an interaction between one of the protons from a methyl group and the Fe_d ($d_{C–Fe}$ = 2.409 Å), consistent with an anagostic interaction.[38]

EPR spectra of [**1**]BF_4 as a solution in toluene-THF were recorded at −150 and 30 °C (Figure 3). The low-temperature spectrum is characteristic of an axial symmetry with g = 2.105 and 2.013. For both *D. desulfuricans* (*Dd*) H_2ase and *C. pasteurianum* (*Cp*) H_2ase I, g_1 = 2.10 was reported, which is very similar to the g_1 value for [**1**]BF_4 of 2.105. However, the g_3 value of 2.013 for [**1**]BF_4 deviates from the g_3 values for *Dd* H_2ase and *Cp* H_2ase I: 1.999 and 2.00, respectively.[39] In comparison to other synthetic H_{ox} models, [**1**]BF_4 g values match well with those of [Fe_2(pdt)$(CO)_3$(dppv)(P*i*-Pr_3)]-BF_4.[30] Hyperfine coupling, assigned to A(^{31}P), is well resolved. In the isotropic spectrum, a triplet is observed at g_{iso} = 2.045 with A(^{31}P) = 70 MHz. The hyperfine splitting is consistent with the spin residing on a single Fe(dppv) center. No hyperfine coupling to the dppv on the nonrotated Fe was resolved, consistent with little delocalization.

Characterization of [*t*-HFe_2(Me_2pdt)$(CO)_2$(dppv)$_2$]$^+$

Like related diiron(I) complexes,[18] [**1**]^0 is protonated by HBF_4 to give a hydride complex (Scheme 3). The salt [*t*-HFe_2(Me_2pdt)$(CO)_2$(dppv)$_2$]BF_4 ([*t*-H**1**]BF_4) was isolated as a brown-green powder and characterized spectroscopically. Its room-temperature ^{31}P NMR spectrum shows four resonances (Figure S15). Consistent with the low symmetry of the complex, the four resonances indicate apical-basal dppv on the proximal iron and a dibasal

dppv on the FeH (Fe_d) center. The locations of the four phosphine ligands are similar for [**1**]BF_4 and [*t*-H**1**]BF_4, consistent with a biomimetic relationship between oxidized and protonated states. Solutions of [*t*-H**1**]BF_4 isomerize, albeit slowly, at room temperature (see the isomerization section). The slowness of this isomerization reflects the effect of steric congestion.[40] The nature of the steric congestion was probed by 1D nuclear Overhauser effect (nOe) NMR spectroscopy (Figure 4). Irradiation of the *t*-H signal at δ −2.23 revealed interactions between the hydride and methyl protons (δ 0.6) and between the hydride and one aryl proton (δ 7.8). Only the axial methyl interacts with the hydride. The DFT-optimized $CH_{Me}\cdots H_tFe_d$ distance is ~1.7 Å. Additionally, the hydride is also close to a pair of aryl protons on the distal dppv; the closest DFT-optimized $CH_A\cdots H_tFe_d$ distance is ~2.3 Å (see Figure 6a and further details on the DFT modeling below).

Isomerization of [*t*-$HFe_2(Me_2pdt)(CO)_2(dppv)_2$]$BF_4$

As for all other examples of [*t*-$HFe_2(SR)_2(CO)_{6-x}L_x]^+$, [*t*-H**1**]$^+$ isomerizes irreversibly to a bridging hydride.[41] The decay rate follows first-order kinetics ($k = 6.0 \times 10^{-4}$ s^{-1}) with a half-life of 19.3 min at 40.3 °C (Figure 5). In contrast, the isomerization of the unmethylated analogue [*t*-$HFe_2(pdt)(CO)_2(dppv)_2]^+$ proceeds with a half-life of minutes at room temperature (k =0.001 s^{-1}).[40] These disparate rates correspond to a difference in free energy of activation of about 1 kcal/mol.

The final product of the isomerization of [*t*-H**1**]$^+$ is the bridging hydride [μ-H**1**]$^+$. Throughout the conversion a third hydride was observed, an intermediate in the isomerization. Its chemical shift at δ −3.63 indicates that this intermediate is a terminal hydride.[40,42] It is C_s-symmetric, as indicated by two ^{31}P NMR signals (δ 79.9 and 72.7; see Figures S20 and 21). These chemical shifts are consistent with dibasal dppv ligands; in contrast, when dppv spans apical-basal sites, the apical phosphines typically absorb near δ 90[40,42]). The intermediate is only observed during isomerization but does not accumulate. It thus appears that [*t*-H**1**]$^+$ converts to a second terminal hydride ([*t*-H**1**′]$^+$), which then converts to the μ-hydride (Scheme 4).

Previous DFT analysis indicated that only the Fe with the hydride twists via a Ray–Dutt mechanism to form the μ-hydride.[43] Analysis of the isomerization of [*t*-$HFe_2(pdt)$-$(CO)_2(dppv)_2]^+$ revealed that the symmetric terminal hydride is approximately 3 kcal/mol higher in energy than the asymmetric analogue.[42] Thus, it is proposed that the isomerization starts with a twist at the Fe_p center to give a C_s-symmetric terminal hydride species. Subsequently, the Fe_d center rotates to give the μ-hydride. These measurements provide evidence for involvement of the proximal (non-hydride-containing) iron in the isomerization of the hydride. The rotation of the $Fe_d(CO)(dppv)H$ center shifts the hydride ligand to the bridging site and the $dppv_d$ to apical-basal positions.[43] By first forming [*t*-H**1**′]$^+$, the cation is preorganized to generate the correct isomer of [μ-H**1**]$^+$, wherein the hydride is trans to a CO ligand, a favored geometry.[43] This result implies that the flexibility of Fe_p influences the isomerization of terminal to bridging hydrides. A similar sequence of events was also seen in [*t*-$HFe_2(adt)(CO)_2(PMe_3)_4]^+$, where the kinetically favored isomer akin to [*t*-H**1**]$^+$ converts partially to an all-basal isomer structurally analogous to [*t*-H**1**′]$^+$.[44]

For the purpose of evaluating their vibrational spectra, [*t*-H^{57}**1**]BF_4, [*t*-D^{57}**1**]O_2CCF_3, [μ-H^{57}**1**]O_2CCF_3, and [μ-D^{57}**1**]-O_2CCF_3 were analyzed. CF_3CO_2D was selected as a convenient source of D^+. Deuteration was incomplete but sufficient for unambiguous assignments.

DFT Modeling of the Structures and Energies of [*t*-H1]$^+$ and [μ-H1]$^+$

Density functional theory (DFT) was applied to elucidate structures and relative energies of the terminal and bridging hydride species. In the absence of their structural determinations, X-ray data on the similar complex [*t*-$HFe_2(adt^{NH2})(CO)_2(dppv)_2](BF_4)_2$[18] has been used to generate starting structures for the models, replacing the NH_2 bridgehead to Me_2pdt^{2-}. The analysis included the two flippamers[30] for the Me_2pdt^{2-} bridgehead, denoted respectively as "d/p" depending on its orientation toward either $Fe_{d/p}$. The optimized structures of the 2 × 2 = 4 isomers are shown in Figure 6 and Figure S50 along with their notations used below in the text. Tables S2 and S3 provide the structural parameters of the diiron cores and relative energies.

Several computational schemes predict that the bridging hydride models [$\mu_{d/p}$-H**1**]$^+$ are 5–16 kcal/mol more stable in comparison to the terminal hydride models [$t_{d/p}$-H**1**]$^+$, regardless of the flippamer (Figure 6 and Table S3). Earlier calculations on [FeFe]-H_2ase indicated 8–16 kcal/mol stabilization for the μ-H vs *t*-H species.[15,45,46] Notably, the [$t_{d/p}$-H**1**]$^+$ models yield metal–ligand distances Fe_d–C_μ = 1.8 Å and Fe_p–C_μ = 2.4–2.6 Å, which reproduce the markedly asymmetric character of the semi-bridging CO binding observed in model complexes and [FeFe]-H_2ase active site.[1] Moderate $Fe_{d/p}$–H_μ distance asymmetries within ~0.1 Å were obtained for the bridging hydride [$\mu_{d/p}$-H**1**]$^+$ models. For every isomer, the optimization produced two or three $CH_X\cdots H_{t/\mu} < 3$ Å interactions involving a hydride, where *X* implies alternatively alkyl protons of either $-CH_3$ (for [t_d-H**1**]$^+$) or $-CH_2-$ (for [t_p-H**1**]$^+$) at Me_2pdt^{2-} and aryl protons (for all the hydride alternatives [*t*/$\mu_{d/p}$-H**1**]$^+$) at Ph as shown in Figure 6.

Computational analysis further revealed that the [t_d-H**1**]$^+$ flippamer is stabilized by 3–5 kcal/mol in comparison to [t_p-H**1**]$^+$. This stabilization may arise in part from the $CH_{Me}\cdots H_tFe_d \approx 1.7$ Å interaction (Figure 6a). Comparable interactions are invoked in isoelectronic [FeFe]-H_2ase models which feature NH···HFe distances of 1.4–2.0 Å.[1,15] The optimized Fe_p–C_μ distance is 0.2 Å shorter in [t_d-H**1**]$^+$ vs in [t_p-H**1**]$^+$ (Table S2). These calculations highlight the sensitivity of the Fe_p–C_μ interactions to subtle changes elsewhere in the molecule, as well as to the DFT methodology.[14] In contrast to [$t_{d/p}$-H**1**]$^+$, the flippamers [$\mu_{d/p}$-H**1**]$^+$ of the bridging hydride isomer are predicted to be essentially equal in energy with the calculated energy gaps within 1.6 kcal/mol.

NRVS and DFT Vibrational Characterization of [*t*-H1]$^+$, [*t*-D1]$^+$, [μ-H1]$^+$, and [μ-D1]$^+$

With thermally stable ^{57}Fe-labeled terminal diiron hydride and its bridging hydride isomer in hand in the forms of [*t*-H/D^{57}**1**]$^+$ and [μ-H/D^{57}**1**]$^+$, their ^{57}Fe–H/D vibrational signatures were characterized by ^{57}Fe NRVS.[47,48] NRVS, which is sensitive only to the motion of ^{57}Fe nuclei, is presented as ^{57}Fe partial vibrational density of states (PVDOS) spectra. NRVS data collected for the four samples [*t*-H^{57}**1**]BF_4, [*t*-D^{57}**1**]O_2CCF_3, [μ-H^{57}**1**]O_2CCF_3, and [μ-

D[57]**1**]-O_2CCF_3 (Figure 7a,d and Figure S51a–d) were interpreted using DFT-calculated ^{57}Fe-PVDOS spectra (Figure 7b,e and Figure S51a–d). The analysis is facilitated by plotting the contributions of hydride vs deuteride to the normal mode energies, provided in Figures 7c,f and Figure S52b as DFT-based $H_{t/\mu}/D_{t/\mu}$-PVDOS. Normal modes having significant H/D-PVDOS are marked in Figure 7c,f and shown in Figure 8 in arrow-style representations.

Weak ^{57}Fe motion and higher frequencies make Fe–H vibrational modes particularly difficult to observe. Additional challenging factors for NRVS presently included (i) only 50% enrichment with ^{57}Fe which effects in higher noise level and (ii) incomplete deuteration (see above). The DFT analysis considered the two Me_2pdt^{2-} d/p-flippamer alternatives for both [*t*-H[57]**1**]$^+$ and [μ-H[57]**1**]$^+$. Here, we restricted our attention to the ~600–800 cm^{-1} "active window", mostly exclusive to the low-intensity NRVS bands based in the δ(^{57}Fe–H/D) bending (δ) vibrations.

As seen in NRVS studies of related complexes,[12,14,15,17,49–54] the spectra exhibit intense bands associated with mixed $^{57}Fe_{d/p}$-S/P/C modes <470 cm^{-1} and $\nu/\delta(Fe_{d/p}$-CO) stretching (ν) and bending (δ) modes in the ~500–600 cm^{-1} region. These higher intensity NRVS bands <600 cm^{-1}, dominated by motions of the ^{57}Fe ligands heavier than hydrides, are discussed in the Supporting Information.

NRVS spectra for [*t*-H[57]**1**]$^+$ exhibit multiple features in the 700–800 cm^{-1} region (Figure 7a), where our DFT calculations on [t_d-H[57]**1**]$^+$ predict two well-defined $\delta(Fe_d$-$H_t)$ modes at 749 and 789 cm^{-1} (Figures 7b,c and 8a) and H_t moves in two perpendicular directions; these modes bear both similarity to and difference from the $^{57}Fe_d$–H bends characterized recently in [FeFe]-H_2ases (see Figure S53 and supplementary discussions in the Supporting Information).[14,15,55] However, the relative [*t*-H[57]**1**]$^+$ vs [*t*-D[57]**1**]$^+$ intensity levels observed in this region are indicative of the isotope sensitivity, and regional maxima at 723 (NRVS) vs 749 cm^{-1} (DFT) match their intensities relatively well. The situation is quite different for [*t*-D[57]**1**]$^+$, producing a band at 601 cm^{-1} which is missing in the spectrum of [*t*-H[57]**1**]$^+$ (Figure 7a). The DFT-calculated ^{57}Fe-PVDOS for [t_d-D[57]**1**]$^+$ predicts a matching band at 604 cm^{-1} produced by modes at 599 and 606 cm^{-1}, resulting from the coupled $\delta(Fe_d$–$D_t)/\delta$(Fe–CO) bending motions (Figures 7b,c and 8b). The δ(Fe–D)/δ(Fe–CO) coupling is responsible for significant amplification of otherwise pure δ(Fe–D) mode intensities and is well-known to enhance the diagnostic power of NRVS on iron hydrides.[14,15,54] In contrast with the 604 cm^{-1} band produced by [t_d-D[57]**1**]$^+$, DFT modeling for another [t_p-D[57]**1**]$^+$ flippamer produces an additional band at 621 cm^{-1} which does not fit the experiment (Figure S51b). Among the two flippamer alternatives, the [t_d-D[57]**1**]$^+$ modeling clearly provides a better fit to the observed NRVS data and therefore the d-flippamer spectra were used as representative in Figure 7b; importantly, this preference is consistent with the computed [$t_{d/p}$-H[57]**1**]$^+$ relative energies favoring [t_d-H[57]**1**]$^+$ and the nOe experimental results on [*t*-H[57]**1**]$^+$ (see the previous sections and Table S3). Interestingly, in spite of the tight $CH_{Me}\cdots H_tFe_d \approx 1.7$ Å dihydrogen contact achieved in [t_d-H[57]**1**]$^+$ (Figure 6a), this interaction does not yield any significant vibrational coupling between the H_{Me} and H_t nuclei (see Figures S52b,c and S53 and supplementary discussions in the Supporting Information).

For the bridging hydride complex, a doublet feature is observed at 694/702 cm^{-1} in the spectrum of [μ-H^{57}**1**]$^+$ (Figure 7d). A similar doublet feature is calculated at 670/687 cm^{-1} for [μ_p-H^{57}**1**]$^+$ (Figure 7e). Mixed ω(Fe$_d$–H$_{\mu}$–Fe$_t$) out-of-plane bending, or wagging (ω), modes absorb at these energies: see e.g. the calculated modes at 670 and 692 cm^{-1} indicated in Figure 7f and shown in Figure 8c. In contrast, [μ_d-H^{57}**1**]$^+$ modeling produces a relatively pure ω(Fe$_d$–H$_{\mu}$–Fe$_t$) wag at 724 cm^{-1} (Figure S51c), which is not consistent with the observed spectra. The DFT spectra for the bridging hydride species in Figure 7e therefore assumed the presence of the p-flippamer absorbing in the ~600–800 cm^{-1} "active window" (see the Supporting Information for an extended discussion).

The [μ_p-D^{57}**1**]$^+$ model produces a red-shifted ω(Fe$_d$–D$_{\mu}$–Fe$_p$) wag at 590 cm^{-1} (Figures 7f and 8d), having vibrational energy similar to that of the δ(Fe$_d$–D$_t$) bends from the [t_d-D^{57}**1**]$^+$ model as discussed above. The ω(Fe$_d$–H$_{\mu}$/D$_{\mu}$–Fe$_p$) wags, however, contain much less H^-/D^- vibrational energy (Figure 7c,f) and show smaller H^-/D^- displacements (Figure 8) in comparison to the δ(Fe$_d$–H$_t$/D$_t$) bends, and therefore H_{μ}^- to D_{μ}^- exchange introduces only a minor perturbation of the δ(Fe–CO) bands for the bridging hydride isomer (Figure 7d,e). DFT rationalizes this behavior as respectively stronger vs weaker involvement of the ^{57}Fe nuclei in the δ(Fe$_d$–H$_t$/D$_t$) bending vs ω(Fe$_d$–H$_{\mu}$/D$_{\mu}$–Fe$_p$) wagging motion, consistent with ~0.2 Å shorter Fe–H distances in [t-H**1**]$^+$ vs [μ-H**1**]$^+$ (Table S2). Calculations therefore rationalize the well-defined NRVS modification between the terminal and bridging species as exposed by the H^- to D^- isotope exchange, which is marked by a dashed red line at ~600 cm^{-1} in Figure 7.

Figure 7d reveals overlapping [μ-H^{57}**1**]$^+$ and [μ-D^{57}**1**]$^+$ NRVS features at 694/702 cm^{-1}, consistent with the [μ-D^{57}**1**]O_2CCF_3 sample contamination by [μ-H^{57}**1**]O_2CCF_3 as quantified by ^{1}H NMR (see above). The corresponding 670–690 cm^{-1} doublet features from the DFT modeling of the *pure* species are however not completely eliminated by the H/D isotope exchanges regardless of the flippamers: see Figure 7b,e and Figure S51a–d. The calculations indicate that these bands, protruding into the δ(^{57}Fe–H) "active window", are produced by many mixed modes of Me_2pdt^{2-}, dppv, and aryl molecular fragments. These modes overlap with the hydride motion only in [μ_p-H^{57}**1**]$^+$ (see the 670 and 692 cm^{-1} modes indicated in Figure 7f and shown in Figure 8c and also the discussion on ω(Fe$_d$–H$_{\mu}$–Fe$_p$) above).

CONCLUSIONS

In this work, a sterically congested diiron hydride complex was prepared as a model for a diferrous hydride state of the [FeFe]-hydrogenases. The steric effects were introduced by combining a pair of dppv ligands and 2,2-dimethylpropane-1,3-dithiolate. The preparative methods were adapted to allow introduction of ^{57}Fe for NRVS analysis. The considerable steric effects are manifested at many stages in the chemistry: ring current effects are seen in the ^{1}H NMR spectrum of [**1**]^0, the 210 mV greater reducing power for [**1**]^0, the enhanced stability of [**1**]$^+$, the nOe interaction between the hydride, dithiolate, and diphosphine in [t-H**1**]$^+$, the slow isomerization of [t-H**1**]$^+$, and the detection of its second isomer [t-H**1**′]$^+$. The last species served as a precursor to the bridging hydride [μ-H**1**]$^+$ isomer, predicted by DFT to be 5–16 kcal/mol more stable than [t-H**1**]$^+$.

Owing to their thermal stability, the salts of respectively [t-H^{57}**1**]$^+$ and [μ-H^{57}**1**]$^+$ are well suited for their comparative assessment by NRVS spectroscopy. The Fe–H/D NRVS bands in the ~600–800 cm^{-1} "active window", in spite of their inherently low intensities, reveal important chemical information when they are rationalized by DFT modeling. The combined application of NRVS and DFT clearly discriminated between the terminal vs bridging hydride isomeric species that differ by the first-shell ligand arrangement in the diiron core. The 720–800 cm^{-1} bands produced by two perpendicular bending δ(Fe–H) motions in [t-H^{57}**1**]$^+$ are twice as intense as the 670–700 cm^{-1} bands produced by wagging ω(Fe–H–Fe) motion in [μ-H^{57}**1**]$^+$. For the deuteride samples, the higher NRVS intensity δ(Fe–CO) bands at ~600 cm^{-1} are noticeably perturbed in [t-D^{57}**1**]$^+$ but not in [μ-D^{57}**1**]$^+$. Analogous NRVS fingerprints supported our assignment of the catalytic H_{hyd} state in [FeFe]-H_2ase to the terminal Fe_d(II)–H hydride species (see ref 15; specifically, Figure S15). The δ(Fe–H) NRVS bands around 750 cm^{-1} have been indicated in H_{hyd} as well by an independent DFT modeling.[55] Using techniques different from NRVS, others proposed bridging hydrides (Fe_p–H–Fe_d) for the H_{sred} and H_{red} states.[7,19]

Analysis of the δ(Fe–H/D) and ω(Fe–H/D–Fe) bands for [t-H/D^{57}**1**]$^+$ and [μ-H/D^{57}**1**]$^+$ gave insights into the orientation of the Me_2pdt^{2-} bridge. The ^{57}Fe-PVDOS spectral signatures for the terminal vs bridging hydride isomers are distinctive because of the presence or absence of $H_X\cdots H_{t/\mu}$ interactions. From the NRVS data, one can infer a considerable level of structural insight. Consistent with the NRVS and nOe experiments rationalized by the DFT calculations, a closed $CH_{Me}\cdots H_tFe_d \approx 1.7$ Å contact is stabilized in the best-fit conformer of [t-H**1**]$^+$. The $CH_{Me}\cdots H_tFe_d$ interaction is reminiscent of the $NH\cdots HFe_d \approx 2.0$ Å dihydrogen interaction characterized recently for the H_{hyd} hydride state of [FeFe]-H_2ase.[15] In contrast to [t-H**1**]$^+$, the dihydrogen interaction in the catalytic H_{hyd} state additionally exhibits vibrational coupling between the two H nuclei.

EXPERIMENTAL SECTION

Reactions and manipulations were performed using standard Schlenk techniques or in a nitrogen atmosphere glovebox. HPLC-grade solvents were dried by filtration through activated alumina or distilled under nitrogen over an appropriate drying agent and then used. ESI-MS data for compounds were acquired using a Waters Micromass Quattro II spectrometer. ^{1}H NMR (500 MHz) and ^{2}H NMR (600 MHz) spectra were referenced to residual solvent relative to TMS. ^{31}P{^{1}H} NMR (202 and 242 MHz) spectra were referenced to external 85% H_3PO_4. Chemical shifts are reported for room temperature in the δ scale. FT-IR spectra were recorded on a PerkinElmer 100 FT-IR spectrometer. Crystallographic data for compounds [**1**]^0 and [**1**]BF_4 were collected using a Siemens SMART diffractometer equipped with a Mo Kα source (λ = 0.71073 Å). *cis*-1,2-Bis(diphenylphosphino)ethylene (dppv) and $HBF_4\cdot Et_2O$ solution were purchased from Aldrich. The compounds Me_2pdtH_2,[56] $Fe_2(Me_2pdt)(CO)_6$, and $Fe_2(Me_2pdt)(CO)_4$(dppv) were prepared according to literature procedures.[20,29]

$Fe_2(Me_2pdt)(CO)_2(dppv)_2$ ([1]^0)

Method 1—A mixture of $Fe_2(Me_2pdt)(CO)_4(dppv)$ (113 mg, 0.15 mmol) and dppv (60 mg, 0.15 mmol) was dissolved in 100 mL of toluene in a Pyrex Schlenk tube. The reaction mixture was irradiated with a 100 W UV immersion lamp (λ = 356 nm, Spectroline) until the reaction was complete (~25 h) as indicated by FT-IR spectroscopy. After the solvent was removed under vacuum, the residue was extracted into 5 mL of CH_2Cl_2. The filtered extract was layered with 50 mL of pentane, and this mixture was stored at −35 °C overnight. The product was precipitated as a greenish black solid. Yield: 103 mg (63%). ^{1}H NMR (500 MHz, CD_2Cl_2): δ 7.71–7.27 (m, 44H, C_6H_5 and =C*H*), 1.33–1.25 (m, 4H, SCH_2), −0.19 (br s, 6H, CH_3). ^{31}P{^{1}H} NMR (CD_2Cl_2): δ 87.2. FT-IR (CH_2Cl_2): ν_{CO} 1898 (vs), 1865 (vs) cm^{-1}. ESI-MS: *m*/*z* 1094.1 [M]$^+$ (calcd 1094.1). Anal. Calcd for $C_{59}H_{54}Fe_2O_2P_4S_2{\cdot}2CH_2Cl_2$ (found): C, 57.93 (58.08); H, 4.62 (4.64).

Method 2—A solution of $Fe_2(Me_2pdt)(CO)_6$ (83 mg, 0.20 mmol) and dppv (158 mg, 0.40 mmol) in 100 mL of dry toluene was irradiated with an LED lamp (λ = 356 nm). The reaction was complete in ~7 h, as indicated by FT-IR spectroscopy. Solvent was removed under vacuum, and the residue was extracted into 5 mL of CH_2Cl_2. The filtered extract was layered with 100 mL of hexane, and the mixture was allowed to stand at −35 °C overnight. The product precipitated as a greenish black solid. Yield: 170 mg (78%).

$[Fe_2(Me_2pdt)(CO)_2(dppv)_2]BF_4$ ([1]BF_4)

A dark green solution of $Fe_2(Me_2pdt)(CO)_2(dppv)_2$ (33 mg, 0.030 mmol) in 2 mL of CH_2Cl_2 was treated at −40 °C with $FcBF_4$ (9 mg, 0.033 mmol) in 3 mL of CH_2Cl_2. The reaction mixture was stirred at −40 °C until the reaction was complete (5 min) as indicated by FT-IR spectroscopy. The resulting solution was then layered with 25 mL of hexane, which was allowed to stand at −35 °C overnight. The product precipitated as blue-black needlelike crystals. Yield: 27 mg (77%). FT-IR (CH_2Cl_2): ν_{CO} 1952 (vs), 1854 (s) cm^{-1}. ^{1}H NMR (500 MHz, CD_2Cl_2): δ 9.40–6.80 (m, 55H, C_6H_5, Ph_2PCH=C*H*PPh_2), 1.26 (m, 4H, 2 × SCH_2), −2.07 (br s, 6H, 2 × CH_3). Anal. Calcd for $C_{59}H_{54}BF_4Fe_2O_2P_4S_2{\cdot}CH_2Cl_2$ (found): C, 56.9 (57.22); H, 4.46 (4.43).

[(*t*-H)$Fe_2(Me_2pdt)(CO)_2(dppv)_2]BF_4$ ([*t*-H1]BF_4)

A dark green solution of $Fe_2(Me_2pdt)(CO)_2(dppv)_2$ (33 mg, 0.030 mmol) in 5 mL of CH_2Cl_2 was treated at 0 °C with $HBF_4{\cdot}Et_2O$ (6.3 μL, 0.045 mmol). This species was not formed when THF was used as the solvent. The reaction mixture was stirred at 0 °C until the reaction was complete (10 min) as indicated by FT-IR spectroscopy. The resulting solution was then layered with 50 mL of hexane, which was allowed to stand at −35 °C overnight. The product, a greenish black solid, was stored at −35 °C in the glovebox. Yield: 15 mg (42%). ^{1}H NMR (500 MHz, CD_2Cl_2): δ 8.22–6.73 (m, 44H, C_6H_5 and =C*H*), 1.59–1.27 (m, 4H, SCH_2), 0.50, 0.03 (s, s, 6H, CH_3), −2.23 (t, J_{PH} = 81 Hz, 1H, (*t*-*H*)Fe). ^{31}P{^{1}H} NMR (CD_2Cl_2, 20): δ 95.3 (s), 87.2 (s), 80.4 (s), 68.7 (s). FT-IR (CH_2Cl_2): ν_{CO} 1964 (vs), 1889 (s) cm^{-1}. ESI-MS: *m*/*z* 1095.1 [M − BF_4]$^+$ (calcd 1095.1). Anal. Calcd for $C_{59}H_{55}BF_4Fe_2O_2P_4S_2{\cdot}2.5CH_2Cl_2$ (found): C, 52.95 (53.01); H, 4.34 (4.38).

[(μ-H)Fe_2(Me_2pdt)(CO)$_2$(dppv)$_2$]BF_4 ([μ-H1]BF_4)

A dark green solution of $Fe_2(Me_2pdt)(CO)_2(dppv)_2$ (44 mg, 0.040 mmol) in 5 mL of CH_2Cl_2 was treated at room temperature with $HBF_4{\cdot}Et_2O$ (8.4 μL, 0.060 mmol). The reaction mixture was stirred at room temperature until the reaction was complete (~41 h) as indicated by FT-IR spectroscopy. After the solvent was removed, the residue was washed with 2 × 10 mL of Et_2O and dried under vacuum. The product was obtained as a brown-red solid. Yield: 35 mg (72%). ^{1}H NMR (500 MHz, CD_2Cl_2): δ 8.08–6.67 (m, 44H, C_6H_5 and =C*H*), 2.57–1.37 (m, 4H, SCH_2), 1.15, 0.20 (s, s, 6H, CH_3), −14.70 (m, 1H, Fe(μ-*H*)Fe). ^{31}P{^{1}H} NMR (CD_2Cl_2, 20 °C): δ 86.8 (s), 81.3 (s), 78.5 (s), 72.5 (s). FT-IR (CH_2Cl_2): ν_{CO} 1974 (broad), 1952 (vs) cm^{-1}. ESI-MS: *m*/*z* 1095.3 [M − BF_4]$^+$ (calcd 1095.1). Anal. Calcd for $C_{59}H_{55}BF_4Fe_2O_2P_4S_2{\cdot}1.5CH_2Cl_2$ (found): C, 55.47 (55.73); H, 4.46 (4.85). The isomerization of [*t*-H**1**]$^+$ to [μ-H**1**]$^+$ was followed at 40.3 °C using ^{31}P NMR spectroscopy. Tri-*p*-tolylphosphine was used as an integration standard.

[(*t*-D)Fe_2(Me_2pdt)(CO)$_2$(dppv)$_2$]BF_4 ([*t*-D1]BF_4)

A dark green solution of $Fe_2(Me_2pdt)(CO)_2(dppv)_2$ (55 mg, 0.050 mmol) in 5 mL of CH_2Cl_2 was treated at 0 °C with D_2O (9.0 μL, 0.050 mmol) followed by $HBF_4{\cdot}Et_2O$ (11.0 μL, 0.075 mmol). The reaction mixture was stirred at 0 °C until the reaction was complete (10 min) as indicated by FT-IR spectroscopy. The resulting solution was then layered with 50 mL of Et_2O, which was allowed to stand at −35 °C overnight. The product precipitated as a greenish black solid and was stored at −35 °C in the glovebox. Yield: 35 mg (59%). The deuteration was incomplete, as indicated by a small *t*-H signal at δ −2.23. ^{1}H NMR (500 MHz, CD_2Cl_2): δ 8.22–6.73 (m, 44H, C_6H_5 and =C*H*), 1.57–1.27 (m, 4H, SCH_2), 0.49, 0.02 (s, s, 6H, CH_3), −2.23 (t, J_{PH} = 80 Hz, 0.3H, (*t*-*H*)Fe). ^{2}D NMR (600 MHz, CH_2Cl_2): δ −2.14 (t, J_{PD} = 12.4 Hz, (*t*-*D*)Fe). ^{31}P{^{1}H} NMR (CD_2Cl_2): δ 95.2 (s), 87.3 (2 × br d), 80.6 (2 × br d), 68.7 (s). FT-IR (CH_2Cl_2): ν_{CO} 1964 (vs), 1890 (s) cm^{-1}. ESI-MS: *m*/*z* 1096.2 [M − BF_4]$^+$ (calcd 1096.2).

[(μ-D)Fe_2(Me_2pdt)(CO)$_2$(dppv)$_2$]BF_4 ([μ-D1]BF_4)

A dark green solution of $Fe_2(Me_2pdt)(CO)_2(dppv)_2$ (33 mg, 0.030 mmol) in 5 mL of CH_2Cl_2 was treated at room temperature with D_2O (5.4 μL, 0.300 mmol) followed by $HBF_4{\cdot}Et_2O$ (12.6 μL, 0.090 mmol). The mixture was stirred at room temperature until the reaction was complete (~52 h) as indicated by FT-IR spectroscopy. The resulting solution was then layered with 25 mL of hexane, which was allowed to stand at −35 °C overnight. The product was obtained as a brown-red solid. Yield: 20 mg (56%). The deuteration was not fully complete, as indicated by a small μ-H signal at δ −14.8. ^{1}H NMR (500 MHz, CD_2Cl_2): δ 8.08–6.68 (m, 44H, C_6H_5 and =C*H*), 260–1.37 (m, 4H, SCH_2), 1.15, 0.21 (s, s, 6H, CH_3), −14.74 (m, 0.3H, Fe(μ-*H*)Fe). ^{2}D NMR (600 MHz, CH_2Cl_2): δ −14.8 (s, Fe(μ-*D*)Fe). ^{31}P{^{1}H} NMR (CD_2Cl_2): δ 86.8 (s), 81.2 (s), 78.4 (2 × br s), 72.5 (s). FT-IR (CH_2Cl_2): ν_{CO} 1974 (broad), 1952 (vs) cm^{-1}. ESI-MS: *m*/*z* 1096.1 [M − -BF_4]$^+$ (calcd 1096.1).

$^{57}FeCl_2$

To a solution of ^{57}Fe powder (250 mg, 4.39×10^{-3} mol) in MeOH (1.6 mL) was added concentrated HCl (12 M, 1.6 mL, 1.92×10^{-2} mol). The reaction mixture was stirred under nitrogen at room temperature for 2 h. The solvent was then removed under vacuum. The residual white powder was dried further by heating under vacuum overnight. The product was used without purification. Yield: 544 mg (97%).

$^{57}Fe(Me_2pdt)(dppv)(CO)_2$

A 100 mL Schlenk flask, equipped with a magnetic stir bar, was charged with $^{57}FeCl_2$ (544 mg, 4.25×10^{-3}), dppv (1.69 g, 4.25×10^{-3}), and THF (30 mL). The reaction mixture was placed under an atmosphere of CO, and the reaction mixture was stirred at room temperature for 2 h. A solution of $Me_2C(CH_2SLi)_2$ (4.25×10^{-3} mol) in THF (10 mL) was generated by treating $Me_2C(CH_2SH)_2$ (576 mg, 4.25×10^{-3} mol) with 4.25 mL of a 1 M solution of BuLi in hexane. This mixture was diluted with MeOH (10 mL) before cannula-transferring to the $^{57}FeCl_2$/dppv mixture. The mixture was stirred at room temperature for 12 h. A dark red, heterogeneous solution formed. The solvents were removed under vacuum, and the residual solid was purified by column chromatography. Elution with CH_2Cl_2 gave a yellow band that was discarded. Subsequent elution with a 5/1 mixture of CH_2Cl_2 and Et_2O gave a red band containing the product. Yield: 719 mg (26%). IR (CH_2Cl_2): ν_{CO} 2014, 1975 cm^{-1}. $^{31}P\{^1H\}$ NMR (CD_2Cl_2): δ 86.1 (dd, J = 35.8, 21.6 Hz), 79.7 (d, $J(^{57}Fe)$ = 38.5 Hz) 59.8, (dd, J = 35.4, 21.6 Hz); ratio 1:17:1. ^1H NMR (500 MHz, CD_2Cl_2): δ 7.96 (d, J = 11.3 Hz, 1H), 7.87 (d, J = 10.7 Hz, 1H), 7.72–7.63 (m, 6H), 7.44 (q, J = 7.7 Hz, 10H), 2.19 (m, 4H), 0.98 (m, 6H).

$(dppv)(CO)^{57}Fe(\mu\text{-}Me_2pdt)Fe(CO)_3$

A toluene (25 mL) solution of $^{57}Fe(Me_2pdt)(dppv)(CO)_2$ (719 mg, 1.12×10^{-3} mol) was treated with a toluene solution of $Fe(bda)(CO)_3$[28] (322 mg, 1.12×10^{-3} mol). The reaction mixture was stirred at room temperature for 16 h, at which point IR spectroscopy indicated that the reaction was complete. The solution was filtered through Celite, and the solvent was removed under vacuum. The residual solid was rinsed with pentane (3 × 10 mL) and dried under vacuum. Yield: 706 mg (87%). IR spectrum (CH_2Cl_2): ν_{CO} 2022, 1953, 1913 cm^{-1}. $^{31}P\{^1H\}$ NMR (CD_2Cl_2): δ 92.83 (d, $J(^{57}Fe)$ = 50.9 Hz), 79.92 (m); ratio 1:0.6. ^1H NMR (500 MHz, CD_2Cl_2): δ 8.16–7.88 (overlapping signals, 4H), 7.78 (m, 1H), 7.67 (m, 1H), 7.57–7.10 (overlapping signals, 16H), 1.72 (m, 2H), 1.29 (m, 2H), 1.08 (s, 3H), 0.09 (s, 3H).

$(dppv)(CO)^{57}Fe(\mu\text{-}Me_2pdt)Fe(CO)(dppv)$ ($[^{57}1]^0$)

A mixture of $(dppv)(CO)^{57}Fe(\mu\text{-}Me_2pdt)Fe(CO)_3$ (120 mg, 1.65×10^{-4} mol) and dppv (66 mg, 1.65×10^{-4} mol) in toluene (100 mL) was irradiated with 356 nm light (LED, 350 mA/m^2). Reaction progress was monitored by IR spectroscopy. After 6 h, irradiation was stopped, and the solvent was removed under vacuum. The crude product was dissolved in a minimum amount of CH_2Cl_2. This extract was layered with pentane, and the mixture was stored at −35 °C overnight. Dark green crystals formed. Yield: 146 mg (83%). FT-IR (CH_2Cl_2): ν_{CO} 1974, 1952, 1897, 1865 cm^{-1}. $^{31}P\{^1H\}$ NMR (CD_2Cl_2): δ 87.21 (br s). ^1H

NMR (500 MHz, CD_2Cl_2): δ 8.13–7.56 (br s, 10H), 7.56–6.72 (broad, overlapping signals, 34H), 1.29 (m, 4H), −0.15 (br s, 6H).

^{57}Fe-Labeled [(t-H)Fe_2(Me_2pdt)$(CO)_2$(dppv)$_2$]BF_4 ([*t*-H^{57}**1**]BF_4)

A CH_2Cl_2 solution of (dppv)(CO)^{57}Fe(μ-Me_2pdt)Fe-(CO)(dppv) (63.4 mg, 5.78×10^{-5} mol) was treated with $HBF_4{\cdot}Et_2O$ (7.9 μL, 9.4 mg, 5.78×10^{-5} mol) at room temperature. A color change from green to green-brown was observed. Solvent was removed under vacuum, and the residual solid was rinsed with THF and Et_2O. Yield: 30 mg (44%). $^{31}P\{^1H\}$ NMR (CD_2Cl_2): δ 95.3 (br s, 1P), 87.3 (br s, 1P), 80.5 (br s), 68.8 (br s, 1P). ^{1}H NMR (500 MHz, CD_2Cl_2): δ 8.68–6.37 (overlapping signals, 44H), 1.59 (m, 2H), 1.30 (m, 2H), 0.53 (s, 3H), 0.05 (s, 3H), −2.20 (t, J = 81 Hz, 1H). ^{1}H NMR analysis of the sample for NRVS revealed a small signal at δ −14.7 corresponding to the presence of ~13% of [μ-H^{57}**1**]BF_4 in this sample (Figure S43).

^{57}Fe-Labeled [(t-D)Fe_2(Me_2pdt)$(CO)_2$(dppv)$_2$]O_2CCF_3 ([t-D^{57}1]O_2CCF_3)

A CH_2Cl_2 solution of (dppv)(CO)^{57}Fe(μ-Me_2pdt)-Fe(CO)(dppv) (63.4 mg, 5.78×10^{-5} mol) was treated with CF_3CO_2D (4.7 μL, 6.6 mg, 5.78×10^{-5} mol). A color change from green to green-brown was observed. Solvent was removed under vacuum, and the residual solid was washed with THF and Et_2O. Yield: 40 mg (58%). $^{31}P\{^1H\}$ NMR (CD_2Cl_2): δ 95.3 (br s, 1P), 87.3 (br s, 1P), 80.5 (br s), 68.8 (br s, 1P). ^{1}H NMR (500 MHz, CD_2Cl_2): δ 8.68–6.37 (overlapping signals, 44H), 1.59 (m, 2H), 1.30 (m, 2H), 0.53 (s, 3H), 0.05 (s, 3H).

^{57}Fe-Labeled [(μ-H)Fe_2(Me_2pdt)$(CO)_2$(dppv)$_2$]BF_4/O_2CCF_3 ([μ-H^{57}1]O_2CCF_3) and [(μ-D)Fe_2(Me_2pdt)$(CO)_2$(dppv)$_2$]O_2CCF_3 ([μ-H^{57}1]O_2CCF_3)

Solutions of [*t*-H^{57}**1**]O_2CCF_3 and [*t*-D^{57}**1**]O_2CCF_3 in 2–4 mL of CH_2Cl_2 were stirred until the IR spectrum showed complete conversion to [μ-H^{57}**1**]$^+$ and [μ-D^{57}**1**]$^+$, respectively. The appearance of an IR band at 1855 cm^{-1} in the spectra of [μ-H^{57}**1**]O_2CCF_3 and [μ-D^{57}**1**]O_2CCF_3 indicates the presence of a small amount of [^{57}**1**]$^+$ in these samples (Figures S44 and S47). Finally, the appearance of a signal at δ −14.7 in the ^{1}H NMR spectrum of [μ-D^{57}**1**]O_2CCF_3 (Figure S49) indicates only 65% deuteration, the remainder being [μ-H^{57}**1**]O_2CCF_3. ^{1}H NMR (500 MHz, CD_2Cl_2): δ 8.08–6.67 (m, 44H, C_6H_5 and =C*H*), 2.57–1.37 (m, 4H, SCH_2), 1.17, 0.23 (s, s, 6H, CH_3), −14.72 (m, 1H, Fe(μ-*H*)Fe). $^{31}P\{^1H\}$ NMR (CD_2Cl_2): δ 87.1 (t), 81.5 (t), 78.8 (t), 72.8 (t). FT-IR (CH_2Cl_2): ν_{CO} 1974 (broad), 1952 (vs) cm^{-1}. [μ-D^{57}**1**]O_2CCF_3. ^{1}H NMR (500 MHz, CD_2Cl_2): δ 8.08–6.67 (m, 44H, C_6H_5 and =C*H*), 2.57–1.37 (m, 4H, SCH_2), 1.17, 0.23 (s, s, 6H, CH_3). $^{31}P\{^1H\}$ NMR (CD_2Cl_2): δ 87.34 (t), 81.8 (t), 78.9 (t), 72.9 (t). FT-IR (CH_2Cl_2): ν_{CO} 1974 (broad), 1952 (vs) cm^{-1}.

Cyclic Voltammetry

Electrochemical experiments were carried out in a nitrogen-filled glovebox fitted with adapters to connect to a CH Instruments Model 600D series electrochemical analyzer. These experiments were conducted in a 3 mL glass cell fitted with a Teflon top. A glassy-carbon electrode (d = 3 mm) was used as the working electrode. A silver wire was used as a pseudoreference electrode, and ferrocene was added to the cell so the collected data could be referenced to the $Fc^{0/+}$ couple (0.00 V). The counter electrode for these experiments was a

platinum wire. Due to these experiments being collected in a glovebox, sparging was not necessary. *iR* compensation was applied to each voltammogram. These experiments were conducted at room temperature with 1 mM of the complex and 0.125 M of supporting electrolyte in dried and deoxygenated solvents.

NRVS

Nuclear resonance vibrational spectroscopy (NRVS) data of [(μ-H/D)^{57}**1**]BF_4/O_2CCF_3 were collected at the Advanced Photon Source (APS) sector 3-ID, Argonne National Laboratory, with the storage ring operating in the standard operating mode (24 electron bunches spaced by 153 ns). A water-cooled high heat-load monochromator (HHLM) consisting of two diamond single crystals with (1,1,1) as the reflection plane and a four-bounce 2Si(4,0,0) × 2Si(10,6,4) high-resolution monochromator (HRM) provided the 14.4 keV X-rays with 1 meV energy resolution. The flux was about 2.5×10^9 photons/s positioned on our sample at the 3ID-D station. The operation temperature was set to 10 K, while the real sample temperature was ~58 K for [(μ-H)^{57}**1**]BF_4 and 62 K for [(μ-D)^{57}**1**]O_2CCF_3. The nuclear scattering induced ^{57}Fe nuclear fluorescence at 14.4 keV, and the converted Fe Kα fluorescence at 6.4 keV was recorded with an Avalanche Photo Diode (APD) detector, with an active area of 10 mm by 10 mm in size and 0.1 mm in thickness.

The NRVS spectra of [(t-H/D)^{57}**1**]BF_4/O_2CCF_3 were collected at SPring-8 BL09XU and BL19LXU in the “C” bunch mode (29 electron bunches spaced by 145.5 ns).[57] The samples were placed in a helium cold finger maintained at 10 K, and the true temperature ranged from 65 to 75 K. Using a double Si(1,1,1) HHLM and a [Ge(4,2,2),2×Si-(9,7,5)] HRM, the nuclear resonance energy at 14.4 keV with a 0.8 meV resolution was achieved (flux = 6×10^9 cps at BL19XU and 2.0×10^9 cps at BL09XU).[17] An APD array was used to detect the ^{57}Fe nuclear fluorescence and Fe Kα fluorescence. [t-D^{57}**1**]O_2CCF_3 was measured using sectional scans: −100 to 550 cm^{-1} at 1 s/pt, 550–800 cm^{-1} at 3 s/pt, 800–1250 cm^{-1} at 1 s/pt, and 1250–1500 cm^{-1} at 20 s/pt with respect to ^{57}Fe nuclear resonance. All NRVS spectra were processed with PHOENIX executed through the web application spectra.tools to yield ^{57}Fe partial vibrational density of states (PVDOS).[58]

DFT Calculations

Structural optimization and normal-mode analysis was done using GAUSSIAN 09,[59] on the basis of the densities exported from single-point calculations using JAGUAR 9.4.[60] The BP86[61,62] (for most of the results) and B3LYP[61] (for single-point energy calculations only) functionals together with the LACV3P** basis set were employed. For the first- and second-row elements, LACV3P** implies 6-311G** triple-ζ basis sets including polarization functions. For the Fe atoms, LACV3P** consists of a triple-ζ quality basis set for the outermost core and valence orbitals and the quasi-relativistic Los Alamos effective core potential (ECP) for the innermost electrons.[63,64] The model environment was considered using a self-consistent reaction field (SCRF) polarizable continuum model and integral equation formalism (IEF-PCM) as implemented in GAUSSIAN 09, with the static dielectric constant set to $\varepsilon = 4.0$ and the remaining IEF-PCM parameters at their default values for water. The calculations (i) including the two-body D3 dispersion corrections by Grimme et al.[65,66] as implemented in GAUSSIAN 09 and (ii) excluding the D3 correction have been

done to generate the normal modes in the (i) <470 cm^{-1} and (ii) >470 cm^{-1} areas, respectively; this combined approach ultimately produced DFT-based ^{57}Fe-PVDOS spectra in better agreement with the experiment. The optimized structures shown in the figures are based on scheme ii, if not otherwise mentioned. On the basis of the normal mode outputs, an in-house Q-SPECTOR program successfully applied previously[15,51–54] was utilized to generate the ^{57}Fe-PVDOS from the normal mode composition factors. An empirical scaling of calculated frequencies has not been applied. The resolution of the observed NRVS spectra was accounted for by convolution of the computed PVDOS intensities with a full width at half-maximum (fwhm) equal to 14 cm^{-1} Lorentzian.

Supplementary Material

Refer to Web version on PubMed Central for supplementary material.

Acknowledgments

Work at Illinois and California was supported by NIH GM-061153 and GM-65440, respectively. Work at Berlin was supported by the Cluster of Excellence “Unifying Concepts in Catalysis” initiative of the DFG. The NRVS were measured at APS (via proposals GUP 49765, 44733, 43032, 39192) and at SPring-8 (via JASRI proposals 2015B1134, 2016B1347, 2016A1154, 2017A1115, 2015A0103-2016A0103 and via RIKEN proposals 20150048, 20160063). We thank Michael Hu, Jiyong Zhao, and Ercan E. Alp, Yoshitaka Yoda, and Kenji Tamasaku for assistance with NRVS measurements.

References

1. Schilter D, Camara JM, Huynh MT, Hammes-Schiffer S, Rauchfuss TB. Hydrogenase Enzymes and Their Synthetic Models: The Role of Metal Hydrides. Chem Rev. 2016; 116:8693–8749. [PubMed: 27353631]
2. Mellor SB, Vavitsas K, Nielsen AZ, Jensen PE. Photosynthetic Fuel for Heterologous Enzymes: The Role of Electron Carrier Proteins. Photosynth Res. 2017; 134:329–342. [PubMed: 28285375]
3. Ash PA, Hidalgo R, Vincent KA. Proton Transfer in the Catalytic Cycle of [NiFe] Hydrogenases: Insight from Vibrational Spectroscopy. ACS Catal. 2017; 7:2471–2485. [PubMed: 28413691]
4. Tard C, Pickett CJ. Structural and Functional Analogues of the Active Sites of the [Fe]-, [NiFe]-, and [FeFe]-Hydrogenases. Chem Rev. 2009; 109:2245–2274. [PubMed: 19438209]
5. Gloaguen F, Rauchfuss TB. Small Molecule Mimics of Hydrogenases: Hydrides and Redox. Chem Soc Rev. 2009; 38:100–108. [PubMed: 19088969]
6. McGrady GS, Guilera G. The Multifarious World of Transition Metal Hydrides. Chem Soc Rev. 2003; 32:383–392. [PubMed: 14671793]
7. Chernev P, Lambertz C, Brünje A, Leidel N, Sigfridsson KGV, Kositzki R, Hsieh C, Yao S, Schiwon R, Driess M, Limberg C, Happe T, Haumann M. Hydride Binding to the Active Site of [FeFe]-Hydrogenase. Inorg Chem. 2014; 53:12164–12177. [PubMed: 25369169]
8. Amara P, Mouesca J-M, Volbeda A, Fontecilla-Camps JC. Carbon Monoxide Dehydrogenase Reaction Mechanism: A Likely Case of Abnormal CO_2 Insertion to a Ni–H^- Bond. Inorg Chem. 2011; 50:1868–1878. [PubMed: 21247090]
9. Lubitz W, Ogata H, Rüdiger O, Reijerse E. Hydrogenases. Chem Rev. 2014; 114:4081–4148. [PubMed: 24655035]
10. Mulder DW, Ratzloff MW, Bruschi M, Greco C, Koonce E, Peters JW, King PW. Investigations on the Role of Proton-Coupled Electron Transfer in Hydrogen Activation by [FeFe]-Hydrogenase. J Am Chem Soc. 2014; 136:15394–15402. [PubMed: 25286239]
11. Winkler M, Senger M, Duan J, Esselborn J, Wittkamp F, Hofmann E, Apfel U, Stripp ST, Happe T. Accumulating the Hydride State in the Catalytic Cycle of [FeFe]-Hydrogenases. Nat Commun. 2017; 8:16115. [PubMed: 28722011]

12. Gilbert-Wilson R, Siebel JF, Adamska-Venkatesh A, Pham CC, Reijerse E, Wang H, Cramer SP, Lubitz W, Rauchfuss TB. Spectroscopic Investigations of [FeFe] Hydrogenase Maturated with $[^{57}Fe_2(adt)(CN)_2(CO)_4]^{2-}$. J Am Chem Soc. 2015; 137:8998–9005. [PubMed: 26091969]
13. Mulder DW, Guo Y, Ratzloff MW, King PW. Identification of a Catalytic Iron-Hydride at the H-cluster of [FeFe]-Hydrogenase. J Am Chem Soc. 2017; 139:83–86. [PubMed: 27973768]
14. Reijerse EJ, Pham CC, Pelmenschikov V, Gilbert-Wilson R, Adamska-Vekatesh A, Siebel JF, Gee LB, Yoda Y, Tamasaku K, Lubitz W, Rauchfuss TB, Cramer SP. Direct Observation of an Iron-Bound Terminal Hydride in [FeFe]-Hydrogenase by Nuclear Resonance Vibrational Spectroscopy. J Am Chem Soc. 2017; 139:4306–4309. [PubMed: 28291336]
15. Pelmenschikov V, Birrell JA, C PC, Mishra N, Wang H, Sommer C, Reijerse E, Richers CP, Tamasaku K, Y Y, Rauchfuss TB, Lubitz W, Cramer SP. Reaction Coordinate Leading to H_2 Production in [FeFe]-Hydrogenase Identified by Nuclear Resonance Vibrational Spectroscopy and Density Functional Theory. J Am Chem Soc. 2017; 139:16894–16902. [PubMed: 29054130]
16. Adamska A, S A, Lambertz C, Rüdiger O, Happe T, Reijerse E, Lubitz W. Identification and Characterization of the “Super-Reduced” State of the H-Cluster in [FeFe]-Hydrogenase: A New Building Block for the Catalytic Cycle? Angew Chem, Int Ed. 2012; 51:11458–11462.
17. Ogata H, Kramer T, Wang H, Schilter D, Pelmenschikov V, van Gastel M, Neese F, Rauchfuss TB, Gee LB, Scott AD, Yoda Y, Tanaka Y, Lubitz W, Cramer SP. Hydride Bridge in [NiFe]-Hydrogenase Observed by Nuclear Resonance Vibrational Spectroscopy. Nat Commun. 2015; 6:7890–7898. [PubMed: 26259066]
18. Carroll ME, Barton BE, Rauchfuss TB, Carroll PJ. Synthetic Models for the Active Site of the [FeFe]-Hydrogenase: Catalytic Proton Reduction and the Structure of the Doubly Protonated Intermediate. J Am Chem Soc. 2012; 134:18843–18852. [PubMed: 23126330]
19. Mebs S, Senger M, Duan J, Wittkamp F, Apfel U, Happe T, Winkler M, Stripp ST, Haumann M. Bridging Hydride at Reduced H-Cluster Species in [FeFe]-Hydrogenases Revealed by Infrared Spectroscopy, Isotope Editing, and Quantum Chemistry. J Am Chem Soc. 2017; 139:12157–12160. [PubMed: 28825810]
20. Wang W, Rauchfuss TB, Moore CE, Rheingold AL, De Gioia L, Zampella G. Crystallographic Characterization of a Fully Rotated, Basic Diiron Dithiolate: Model for the H_{red} State. Chem Eur J. 2013; 19:15476–15479. [PubMed: 24130068]
21. Hsieh C, Erdem Ö, Harman S, Singleton M, Reijerse E, Lubitz W, Popescu CV, Reibenspies JH, Brothers SM, Hall MB, Darensbourg MY. Structural and Spectroscopic Features of Mixed Valent $Fe^{II}Fe^{I}$ Complexes and Factors Related to the Rotated Configuration of Diiron Hydrogenase. J Am Chem Soc. 2012; 134:13089–13102. [PubMed: 22774845]
22. Capon J, Ezzaher S, Gloaguen F, Pétillon FY, Schollhammer P, Talarmin J, Davin TJ, McGrady JE, Muir KW. Electrochemical and Theoretical Investigations of the Reduction of $[Fe_2(CO)_5L\{\mu\text{-}SCH_2XCH_2S\}]$ Complexes Related to [FeFe] Hydrogenase. New J Chem. 2007; 31:2052–2064.
23. Goy R, Bertini L, Elleouet C, Gorls H, Zampella G, Talarmin J, De Gioia L, Schollhammer P, Apfel U, Weigand W. A Sterically Stabilized Fe^{I}-Fe^{I} Semi-Rotated Conformation of [FeFe] Hydrogenase Subsite Model. Dalton Trans. 2015; 44:1690–1699. [PubMed: 25436832]
24. Schilter D, Nilges MJ, Chakrabarti M, Lindahl PA, Rauchfuss TB, Stein M. Mixed-Valence Nickel-Iron Dithiolate Models of the [NiFe]-Hydrogenase Active Site. Inorg Chem. 2012; 51:2338–2348. [PubMed: 22304696]
25. Justice AK, Zampella G, De Gioia L, Rauchfuss TB. Lewis vs. Brønsted-Basicities of Diiron Dithiolates: Spectroscopic Detection of the ″Rotated Structure″ and Remarkable Effects of Ethane- vs. Propanedithiolate. Chem Commun. 2007:2019–2021.
26. Li Y, Rauchfuss TB. Synthesis of Diiron(I) Dithiolato Carbonyl Complexes. Chem Rev. 2016; 116:7043–7077. [PubMed: 27258046]
27. Carroll ME, Chen J, Gray DE, Lansing JC, Rauchfuss TB. Ferrous Carbonyl Dithiolates as Precursors to FeFe, FeCo, and FeMn Carbonyl Dithiolates. Organometallics. 2014; 33:858–867. [PubMed: 24803716]
28. Domingos AJP, Howell JAS, Johnson BFG, Lewis J. Inorg Synth. 1990; 28:52.

29. Singleton ML, Jenkins RM, Klemashevich CL, Darensbourg MY. The Effect of Bridgehead Steric Bulk on the Ground State and Intramolecular Exchange Processes of (μ-$SCH_2CR_2CH_2S$)[$Fe(CO)_3$][$Fe(CO)_2L$] complexes. C R Chim. 2008; 11:861–874.
30. Justice AK, De Gioia L, Nilges MJ, Rauchfuss TB, Wilson SR, Zampella G. Redox and Structural Properties of Mixed-Valence Models for the Active Site of the [FeFe]-Hydrogenase: Progress and Challenges. Inorg Chem. 2008; 47:7405–7414. [PubMed: 18620387]
31. Justice AK, Rauchfuss TB, Wilson SR. Unsaturated, Mixed-Valence Diiron Dithiolate Model for the H_{ox} State of the [FeFe] Hydrogenase. Angew Chem, Int Ed. 2007; 46:6152–6154.
32. Rauchfuss TB. Diiron Azadithiolates as Models for the [FeFe]-Hydrogenase Active Site and Paradigm for the Role of the Second Coordination Sphere. Acc Chem Res. 2015; 48:2107–2116. [PubMed: 26079848]
33. Silakov A, Olsen MT, Sproules S, Reijerse EJ, Rauchfuss TB, Lubitz W. EPR/ENDOR, Mössbauer, and Quantum-Chemical Investigations of Diiron Complexes Mimicking the Active Oxidized State of [FeFe]-Hydrogenase. Inorg Chem. 2012; 51:8617–8628. [PubMed: 22800196]
34. Liu T, Darensbourg MY. A Mixed-Valent, Fe(II)Fe(I), Diiron Complex Reproduces the Unique Rotated State of the [FeFe]Hydrogenase Active Site. J Am Chem Soc. 2007; 129:7008–7009. [PubMed: 17497786]
35. Thomas CM, Liu T, Hall MB, Darensbourg MY. Series of Mixed Valent Fe(II)Fe(I) Complexes that Model the H_{ox} State of [FeFe]Hydrogenase: Redox Properties, Density-Functional Theory Investigation, and Reactivities with Extrinsic CO. Inorg Chem. 2008; 47:7009–7024. [PubMed: 18597449]
36. Tye JW, Darensbourg MY, Hall MB. Refining the Active Site Structure of Iron-Iron Hydrogenase Using Computational Infrared Spectroscopy. Inorg Chem. 2008; 47:2380–2388. [PubMed: 18307282]
37. Wang W, Rauchfuss TB, Zhu L, Zampella G. New Reactions of Terminal Hydrides on a Diiron Dithiolate. J Am Chem Soc. 2014; 136:5773–5782. [PubMed: 24661238]
38. Brookhart M, Green MLH, Parkin G. Agostic Interactions in Transition Metal Compounds. Proc Natl Acad Sci U S A. 2007; 104:6908–6914. [PubMed: 17442749]
39. Silakov A, Reijerse EJ, Albracht SPJ, Hatchikian EC, Lubitz W. The Electronic Structure of the H-Cluster in the [FeFe]-Hydrogenase from *Desulfovibrio desulfuricans*: A Q-band ^{57}Fe-ENDOR and HYSCORE Study. J Am Chem Soc. 2007; 129:11447–11458. [PubMed: 17722921]
40. Barton BE, Rauchfuss TB. Terminal Hydride in [FeFe]-Hydrogenase Model Has Lower Potential for H_2 Production Than the Isomeric Bridging Hydride. Inorg Chem. 2008; 47:2261–2263. [PubMed: 18333613]
41. Filippi G, Arrigoni F, Bertini L, De Gioia L, Zampella G. DFT Dissection of the Reduction Step in H_2 Catalytic Production by [FeFe]-Hydrogenase-Inspired Models: Can the Bridging Hydride Become More Reactive than the Terminal Isomer. Inorg Chem. 2015; 54:9529–9542. [PubMed: 26359661]
42. Barton BE, Zampella G, Justice AK, De Gioia L, Rauchfuss TB, Wilson SR. Isomerization of the Hydride Complexes $[HFe_2(SR)_2(PR3)_x(CO)_{6-x}]^+$ (x = 2, 3, 4) Relevant to the Active Site Models for the [FeFe]-Hydrogenases. Dalton Trans. 2010; 39:3011–3019. [PubMed: 20221534]
43. Zampella G, Fantucci P, De Gioia L. DFT Characterization of the Reaction Pathways for Terminal- to μ-hydride Isomerisation in Synthetic Models of the [FeFe]-Hydrogenase Active Site. Chem Commun. 2010; 46:8824–8826.
44. Zaffaroni R, Rauchfuss TB, Gray DL, De Gioia L, Zampella G. Terminal vs Bridging Hydrides of Diiron Dithiolates: Protonation of Fe_2(dithiolate)$(CO)_2(PMe_3)_4$. J Am Chem Soc. 2012; 134:19260–19269. [PubMed: 23095145]
45. Bruschi M, Greco C, Kaukonen M, Fantucci P, Ryde U, De Gioia L. Influence of the $[2Fe]_H$ Subcluster Environment on the Properties of Key Intermediates in the Catalytic Cycle of [FeFe] Hydrogenases: Hints for the Rational Design of Synthetic Catalysts. Angew Chem, Int Ed. 2009; 48:3503–3506.
46. Finkelmann AR, Stiebritz MT, Reiher M. Inaccessibility of the μ-Hydride Species in [FeFe] Hydrogenases. Chem Sci. 2014; 5:215–221.

47. Sturhahn W, Toellner T, Alp E, Zhang X, Ando M, Yoda Y, Kikuta S, Seto M, Kimball C, Dabrowski B. Phonon Density of States Measured by Inelastic Nuclear Resonant Scattering. Phys Rev Lett. 1995; 74:3832–3835. [PubMed: 10058308]
48. Seto M, Yoda Y, Kikuta S, Zhang X, Ando M. Observation of Nuclear Resonant Scattering Accompanied by Phonon Excitation Using Synchrotron Radiation. Phys Rev Lett. 1995; 74:3828–3831. [PubMed: 10058307]
49. Kamali S, Wang H, Mitra D, Ogata H, Lubitz W, Manor BC, Rauchfuss TB, Byrne D, Bonnefoy V, Jenney FE Jr, Adams MWW, Yoda Y, Alp E, Zhao J, Cramer SP. Observation of the Fe-CN and Fe-CO Vibrations in the Active Site of [NiFe] Hydrogenase by Nuclear Resonance Vibrational Spectroscopy. Angew Chem, Int Ed. 2013; 52:724–728.
50. Guo Y, Wang H, Xiao Y, Vogt S, Thauer RK, Shima S, Volkers PI, Rauchfuss TB, Pelmenschikov V, Case DA, Alp E, Sturhahn W, Yoda Y, Cramer SP. Characterization of the Fe Site in Iron–Sulfur Cluster-Free Hydrogenase (Hmd) and of a Model Compound *via* Nuclear Resonant Vibrational Spectroscopy (NRVS). Inorg Chem. 2008; 47:3969–3977. [PubMed: 18407624]
51. Mitra D, George SJ, Guo YS, Kamali S, Keable S, Peters JW, Pelmenschikov V, Case DA, Cramer SP. Characterization of [4Fe-4S] Cluster Vibrations and Structure in Nitrogenase Fe Protein at Three Oxidation Levels via Combined NRVS, EXAFS, and DFT Analyses. J Am Chem Soc. 2013; 135:2530–2543. [PubMed: 23282058]
52. Mitra D, Pelmenschikov V, Guo YS, Case DA, Wang HX, Dong WB, Tan ML, Ichiye T, Jenney FE, Adams MWW, Yoda Y, Zhao JY, Cramer SP. Dynamics of the [4Fe-4S] Cluster in *Pyrococcus furiosus* D14C Ferredoxin via Nuclear Resonance Vibrational and Resonance Raman Spectroscopies, Force Field Simulations, and Density Functional Theory Calculations. Biochemistry. 2011; 50:5220–5235. [PubMed: 21500788]
53. Yan LF, Pelmenschikov V, Dapper CH, Scott AD, Newton WE, Cramer SP. IR-Monitored Photolysis of CO-Inhibited Nitrogenase: A Major EPR-Silent Species with Coupled Terminal CO Ligands. Chem Eur J. 2012; 18:16349–16357. [PubMed: 23136072]
54. Pelmenschikov V, Guo YS, Wang HX, Cramer SP, Case DA. Fe-H/D Stretching and Bending Modes in Nuclear Resonant Vibrational, Raman and Infrared Spectroscopies: Comparisons of Density Functional Theory and Experiment. Faraday Discuss. 2011; 148:409–420. [PubMed: 21322496]
55. Mebs S, Kositzki R, Duan J, Kertess L, Senger M, Wittkamp F, Apfel U, Happe T, Stripp ST, Winkler M, Haumann M. Hydrogen and Oxygen Trapping at the H-cluster of [FeFe]-Hydrogenase Revealed by Site-Selective Spectroscopy and QM/MM Calculations. Biochim Biophys Acta, Bioenerg. 2018; 1859:28–41.
56. Aggarwal VK, Davies IW, Franklin R, Maddock J, Mahon MF, Molloy KC. Studies on the Oxidation of 1, 3-Dithiane and 5, 5-Disubstituted Analogues Including X-ray Crystal Structure, Equilibration Studies and pKa Measurements on Selected Oxides. J Chem Soc, Perkin Trans. 1(1994):2363–2368.
57. Yoda Y, Yabashi M, Izumi K, Zhang XW, Kishimoto S, Kitao S, Seto M, Mitsui T, Harami T, Imai Y, Kikuta S. Nuclear Resonant Scattering Beamline at SPring-8. Nucl Instrum Methods Phys Res, Sect A. 2001; 467-468:715–718.
58. Sturhahn W. CONUSS and PHOENIX: Evaluation of nuclear resonant scattering data. Hyperfine Interact. 2000; 125:149–172.
59. Frisch, MJ., Trucks, GW., Schlegel, HB., Scuseria, GE., Robb, MA., Cheeseman, JR., Scalmani, G., Barone, V., Mennucci, B., Petersson, GA., Nakatsuji, H., Caricato, M., Li, X., Hratchian, HP., Izmaylov, AF., Bloino, J., Zheng, G., Sonnenberg, JL., Hada, M., Ehara, M., Toyota, K., Fukuda, R., Hasegawa, J., Ishida, M., Nakajima, T., Honda, Y., Kitao, O., Nakai, H., Vreven, T., Montgomery, JA., Jr, Peralta, JE., Ogliaro, F., Bearpark, M., Heyd, JJ., Brothers, E., Kudin, KN., Staroverov, VN., Kobayashi, R., Normand, J., Raghavachari, K., Rendell, A., Burant, JC., Iyengar, SS., Tomasi, J., Cossi, M., Rega, N., Millam, JM., Klene, M., Knox, JE., Cross, JB., Bakken, V., Adamo, C., Jaramillo, J., Gomperts, R., Stratmann, RE., Yazyev, O., Austin, AJ., Cammi, R., Pomelli, C., Ochterski, JW., Martin, RL., Morokuma, K., Zakrzewski, VG., Voth, GA., Salvador, P., Dannenberg, JJ., Dapprich, S., Daniels, AD., Farkas, Ö., Foresman, JB., Ortiz, JV., Cioslowski, J., Fox, DJ. Gaussian 09, Revision D 01. Gaussian Inc; Wallingford, CT: 2009.
60. Jaguar, version 9.4. Schrodinger, Inc.; New York: 2016.

61. Becke AD. Density-Functional Exchange-Energy Approximation with Correct Asymptotic-Behavior. Phys Rev A: At, Mol, Opt Phys. 1988; 38:3098–3100.

62. Perdew JP. Density-Functional Approximation for the Correlation-Energy of the Inhomogeneous Electron-Gas. Phys Rev B: Condens Matter Mater Phys. 1986; 33:8822–8824.

63. McLean AD, Chandler GS. Contracted Gaussian Basis Sets for Molecular Calculations. I. Second Row Atoms, Z = 11–18. J Chem Phys. 1980; 72:5639–5648.

64. Krishnan R, Binkley JS, Seeger R, Pople JA. Self-consistent molecular orbital methods. XX. A Basis Set for Correlated Wave Functions. J Chem Phys. 1980; 72:650–654.

65. Grimme S, Antony J, Ehrlich S, Krieg H. A Consistent and Accurate *Ab Initio* Parametrization of Density Functional Dispersion Correction (DFT-D) for the 94 elements H-Pu. J Chem Phys. 2010; 132:154104. [PubMed: 20423165]

66. Goerigk L, Grimme S. A Thorough Benchmark of Density Functional Methods for General Main Group Thermochemistry, Kinetics, and Noncovalent Interactions. Phys Chem Chem Phys. 2011; 13:6670–6688. [PubMed: 21384027]

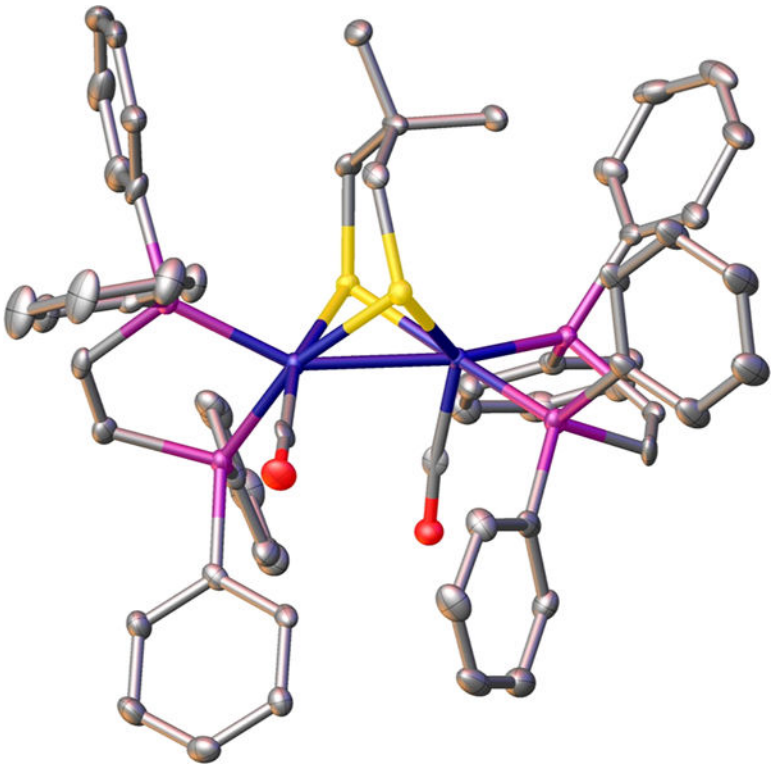

Figure 1.

Solid-state structure of $Fe_2(Me_2pdt)(CO)_2(dppv)_2$ ($[\mathbf{1}]^0$). Disorder in the phenyl rings and solvent is removed for clarity.

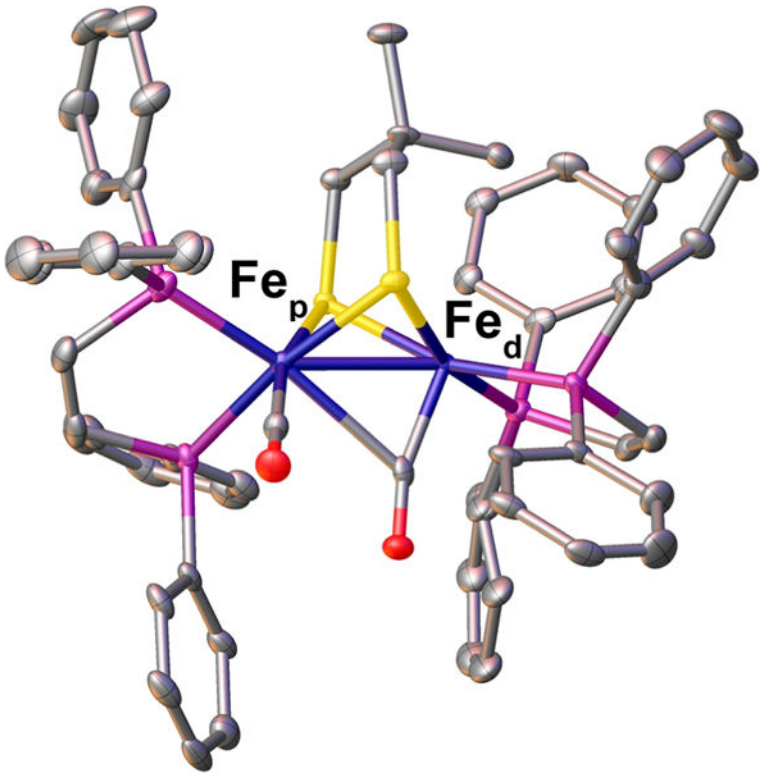

Figure 2.

Crystal structure of $[Fe_2(Me_2pdt)(CO)_2(dppv)_2]BF_4$ ([**1**]BF_4) with thermal ellipsoids drawn at the 50% probability level. Hydrogen atoms and the counteranion are omitted.

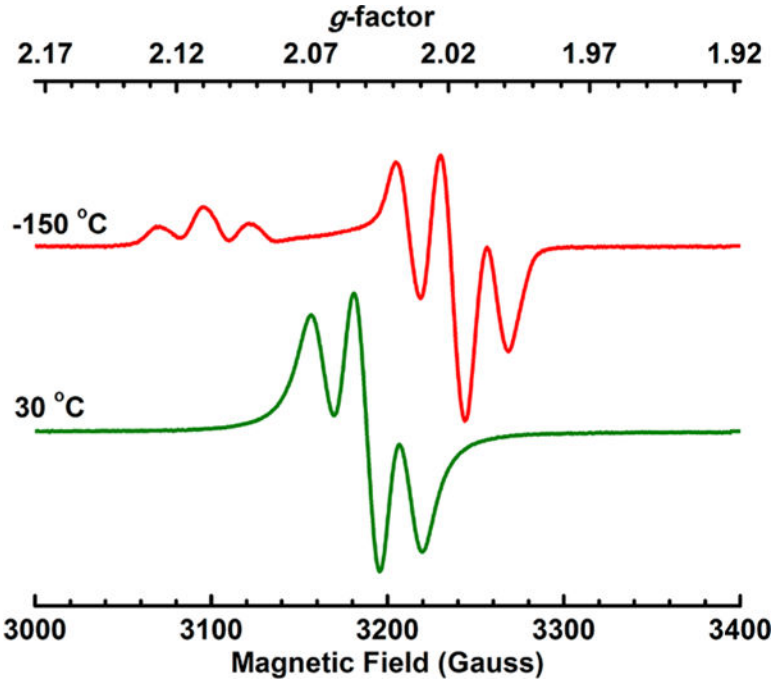

Figure 3.

X-band EPR spectrum of [**1**]BF_4 in 1/1 toluene/THF. The top spectrum was recorded at −150 °C and the bottom spectrum at 30 °C.

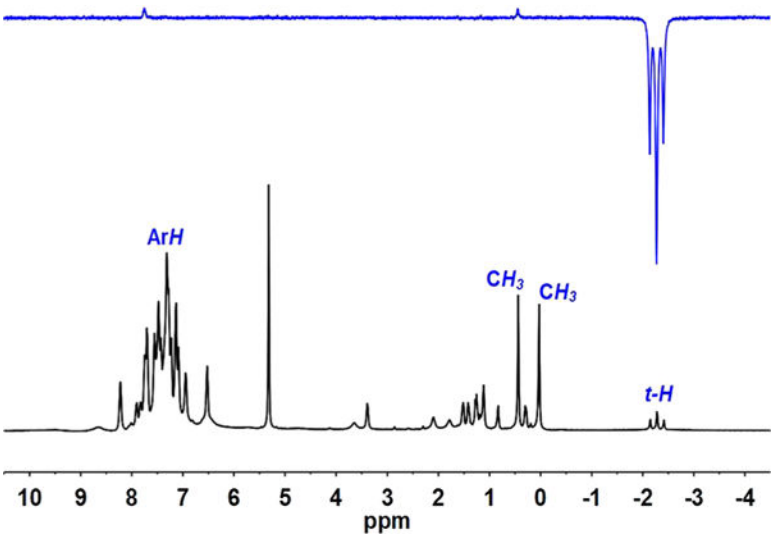

Figure 4.
^{1}H NMR spectrum and nOe spectrum of [*t*-H**1**]BF_4.

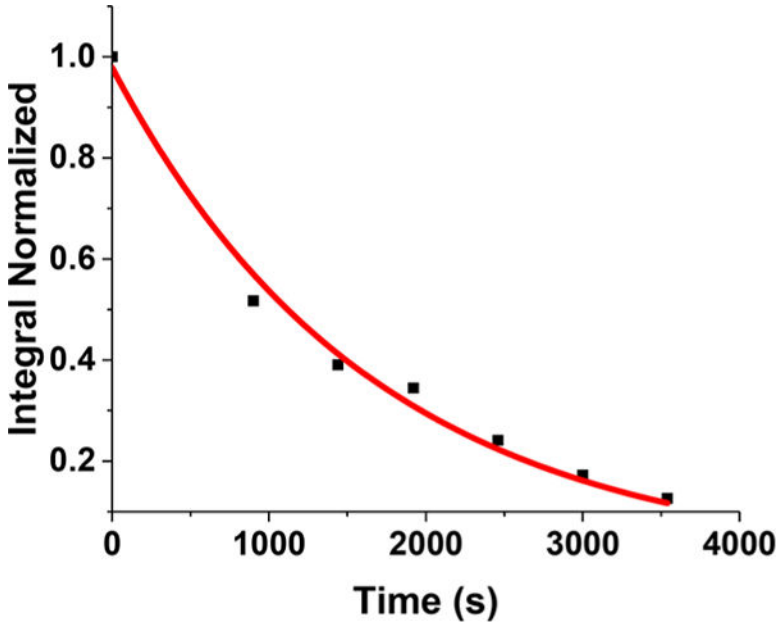

Figure 5.
Kinetic trace of [*t*-H**1**]$^{+}$ isomerization to [μ-H**1**]$^{+}$ as followed by ^{31}P NMR spectroscopy at 40.3 °C.

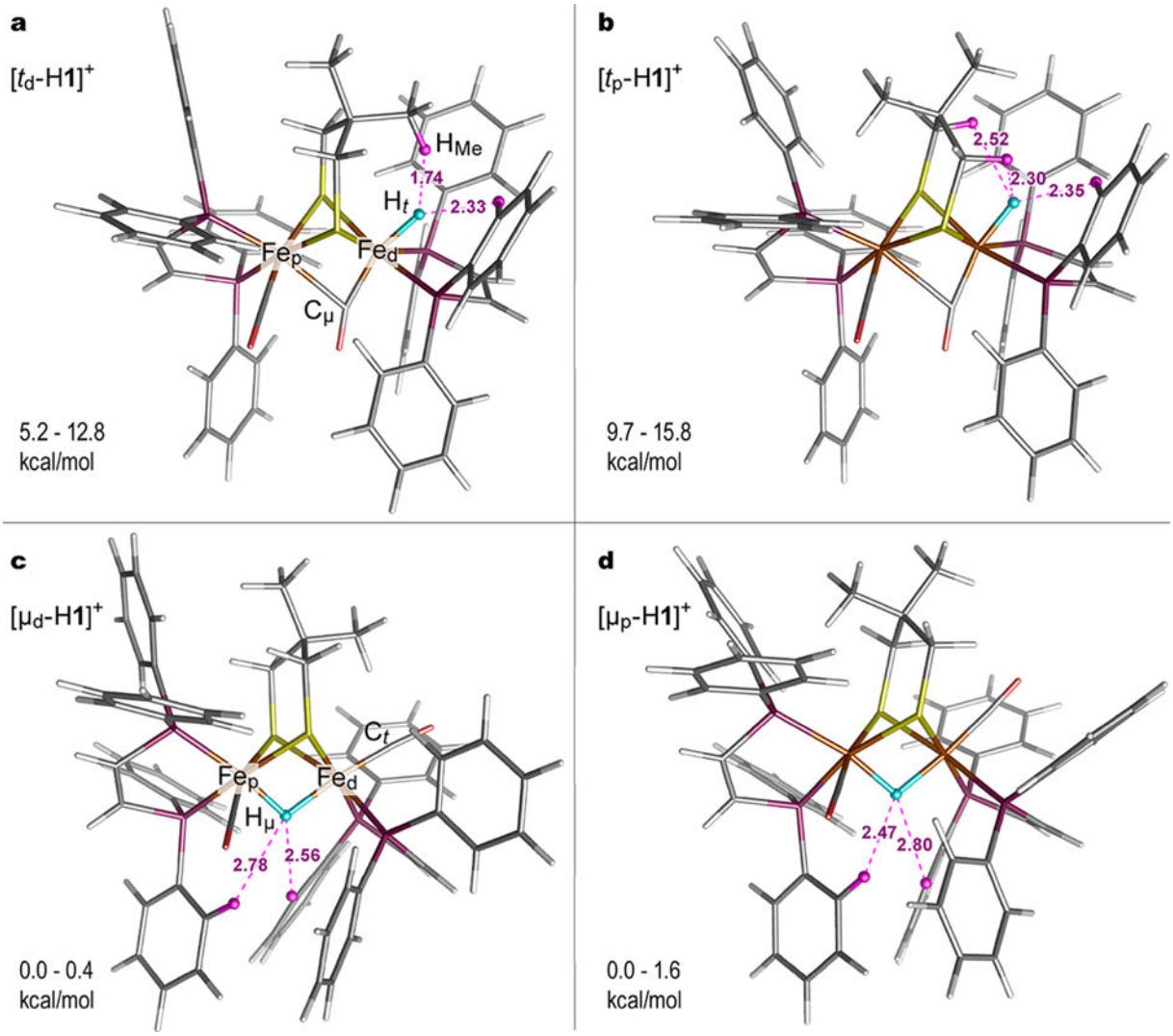

Figure 6.

DFT-optimized structures of the terminal (a, b) and bridging (c, d) hydride isomeric species including their d- (a and c) and p- (b and d) flippamer alternatives on the Me_2pdt^{2-} bridge conformation. Notations of the species are provided ([t_d-H**1**]$^+$, [t_p-H**1**]$^+$, [μ_d-H**1**]$^+$, [μ_p-H**1**]$^+$). Important atomic labels are provided in (a and c). The $H_{t/\mu}$ hydride site is highlighted as a blue sphere. The $CH_X\cdots H_{t/\mu}Fe_d$ dihydrogen contacts within 3 Å are shown, with H_X highlighted as purple spheres. The relative energy ranges provided are based on the values given in Table S3.

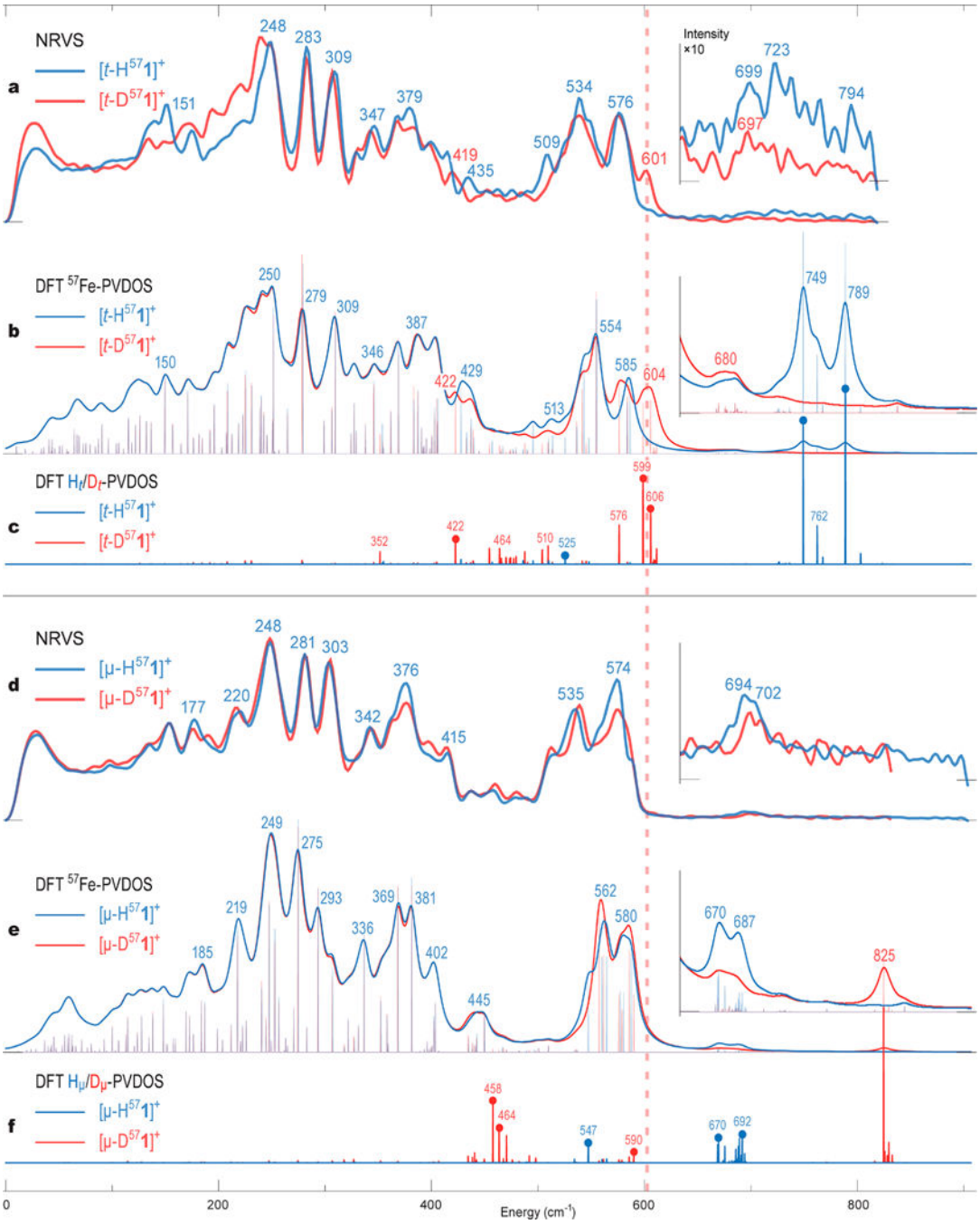

Figure 7.

^{57}Fe-PVDOS vibrational spectra for the H/D variants (correspondingly in blue/red) of the terminal [*t*-H/D^{57}**1**]$^{+}$ (upper panel, a, b) and bridging [μ-H/D^{57}**1**]$^{+}$ (lower panel, d, e) hydride species characterized by NRVS experiments (a, d) and DFT calculations (b, e). The ×10 intensity insets display the spectra >620 cm^{-1}. DFT-based stick-style spectra show PVDOS for the terminal H_t/D_t (c) and bridging H_μ/D_μ (f) hydrides and 2 × $^{57}Fe_{d/p}$ (d, e) iron nuclei. The dashed vertical line at ~600 cm^{-1} indicates the key difference between the [*t*-D^{57}**1**]$^{+}$ and [μ-D^{57}**1**]$^{+}$ spectra as explained in the text. The labels (cm^{-1}) indicate band

positions (a, b, d, e) or individual normal-mode frequencies (c, f). Mode positions marked with thick dots (c, f) correspond to significant H^-/D^- hydride motions; arrow-style molecular representation of these modes is available in Figure 8. See Figure S51 for alternative spectra arrangement and also DFT ^{57}Fe-PVDOS for the d/p-conformers of the Me_2pdt^{2-} bridge.

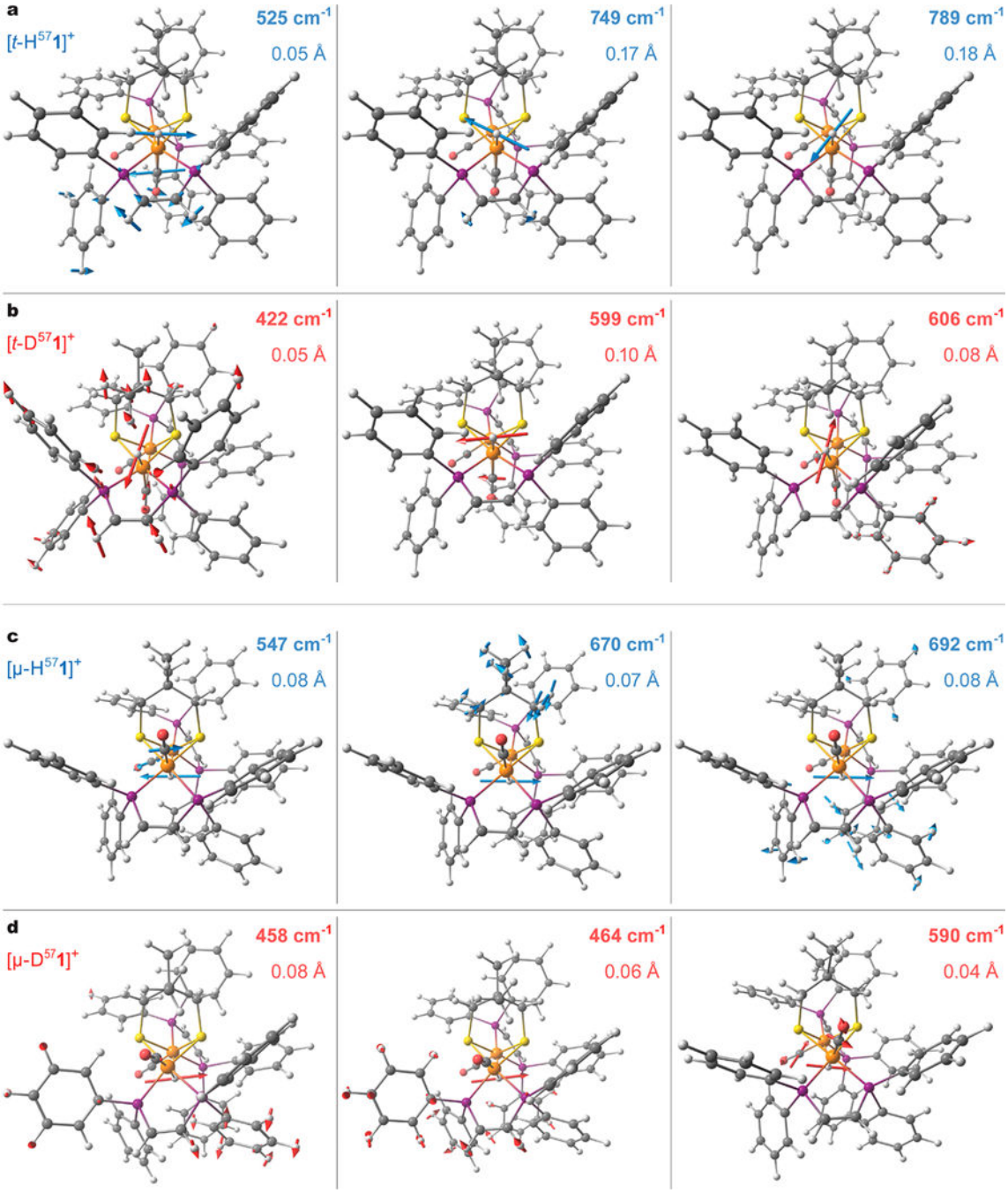

Figure 8.

Arrow-style molecular representation of selected normal modes having significant hydride motion character in the best-fit DFT models for the H/D variants of the terminal [*t*-H/D^{57}**1**]$^{+}$ (a, b) and bridging [μ-H/D^{57}**1**]$^{+}$ (c, d) hydride species. Red/blue coloring of labels and arrows corresponds to the H^{-}/D^{-} hydride isotope alternatives. The computed mode frequencies (cm^{-1}) and the $H/D_{t/\mu}$ hydride nuclei displacement amplitudes (Å) are given. The same modes are marked in the H/D-PVDOS spectra in Figure 7c,f. For these and other vibrational modes animated, see the Supporting Information.

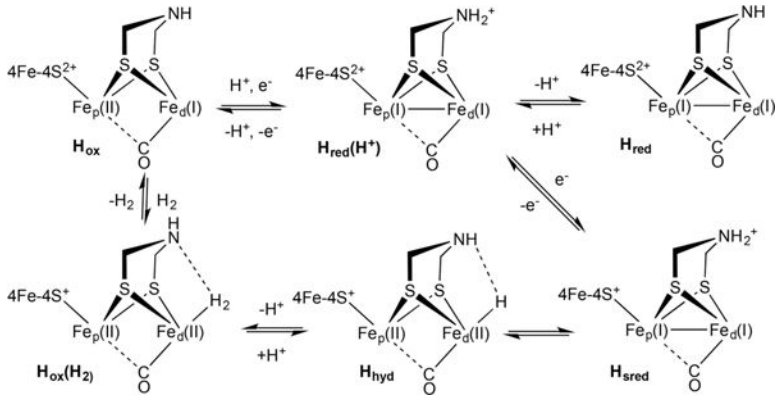

Scheme 1. Proposed Catalytic Cycle of [FeFe]-H_2ase Enzymes Including All States That Have Been Identified in Wild-Type Enzymes and the Proposed H_2 Adduct[a,16]

[a]Terminal CO/CN ligands are omitted for clarity.

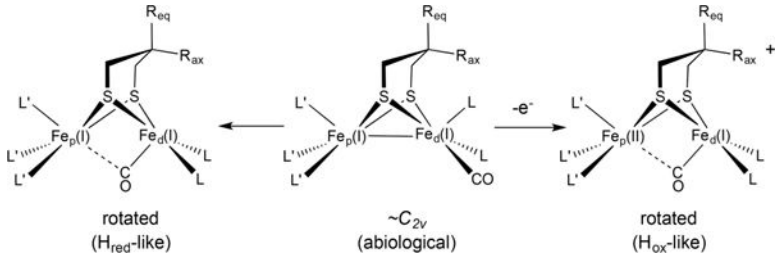

Scheme 2. Compounds of the Type $Fe_2[(SCH_2)_2X]L_6$ Normally Existing as Symmetrical Isomers, with Idealized C_{2v} Structures[a]

[a]They distort to rotated structures upon oxidation or, in some cases, with large ligands and bulky dithiolates even in the absence of redox.

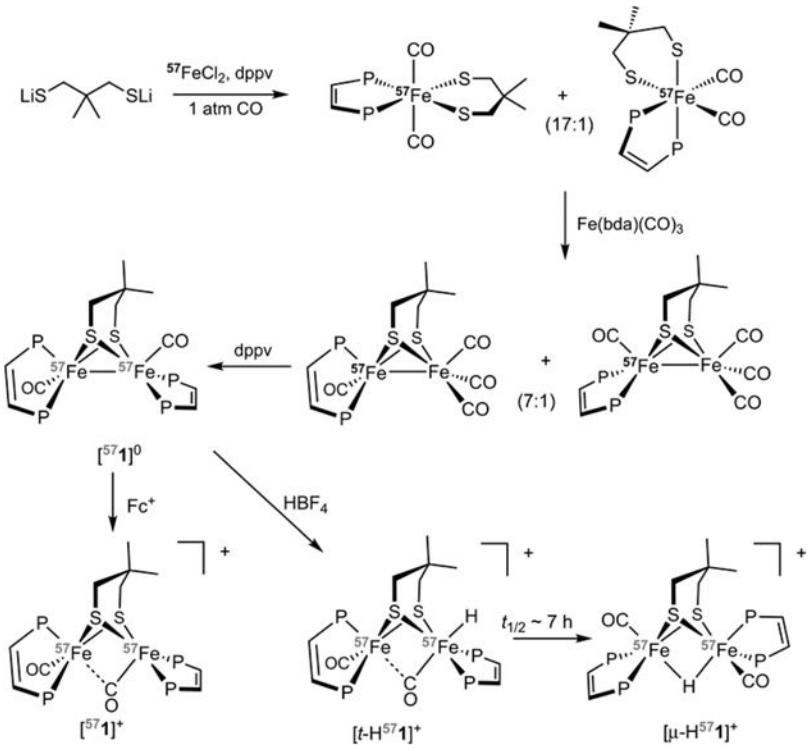

Scheme 3. Synthesis of ^{57}FeFe(Me$_2$pdt)(CO)$_2$(dppv)$_2$ ([^{57}1]^0) and Its Derivatives[a]

[a]Ph groups on phosphorus are omitted for clarity. The number 57 shown in gray implies 50% ^{57}Fe.

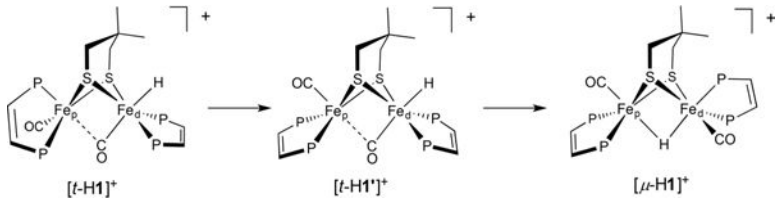

Scheme 4. Proposed Pathway for the Isomerization of [*t*-HFe$_2$(Me$_2$pdt)(CO)$_2$(dppv)$_2$]BF$_4$ to [*μ*-HFe$_2$(Me$_2$pdt)(CO)$_2$(dppv)$_2$]BF$_4$[a]

[a]Ph groups are omitted for clarity.